Available online at www.sciencedirect.com

ScienceDirect

Geochimica et Cosmochimica Acta 207 (2017) 277–297

Geochimica et Cosmochimica Acta

www.elsevier.com/locate/gca

Crystallization history of enriched shergottites from Fe and Mg isotope fractionation in olivine megacrysts

Max Collinet [a,*], Bernard Charlier [b], Olivier Namur [c], Martin Oeser [c], Etienne Médard [d,e], Stefan Weyer [c]

[a] Department of Earth, Atmospheric, and Planetary Science, Massachusetts Institute of Technology, Cambridge, MA 02139, USA
[b] Département de Géologie, Université de Liège, 4000 Sart Tilman, Belgium
[c] Institut für Mineralogie, Leibniz Universität Hannover, 30167 Hannover, Germany
[d] Lunar and Planetary Institute, 3600 Bay Area Boulevard, Houston, TX 77058, USA
[e] Laboratoire Magmas et Volcans, Université Blaise Pascal-CNRS-IRD, 63178 Aubière, France

Received 26 November 2016; accepted in revised form 6 March 2017; Available online 30 March 2017

Abstract

Martian meteorites are the only samples available from the surface of Mars. Among them, olivine-phyric shergottites are basalts containing large zoned olivine crystals with highly magnesian cores (Fo 70–85) and rims richer in Fe (Fo 45–60). The Northwest Africa 1068 meteorite is one of the most primitive "enriched" shergottites (high initial $^{87}Sr/^{86}Sr$ and low initial $\varepsilon^{143}Nd$). It contains olivine crystals as magnesian as Fo 77 and is a major source of information to constrain the composition of the parental melt, the composition and depth of the mantle source, and the cooling and crystallization history of one of the younger magmatic events on Mars (~180 Ma). In this study, Fe-Mg isotope profiles analyzed *in situ* by femtosecond-laser ablation MC-ICP-MS are combined with compositional profiles of major and trace elements in olivine megacrysts. The cores of olivine megacrysts are enriched in light Fe isotopes ($\delta^{56}Fe_{IRMM-14} = -0.6$ to $-0.9‰$) and heavy Mg isotopes ($\delta^{26}Mg_{DSM-3} = 0–0.2‰$) relative to megacryst rims and to the bulk martian isotopic composition ($\delta^{56}Fe = 0 \pm 0.05‰$, $\delta^{26}Mg = -0.27 \pm 0.04‰$). The flat forsterite profiles of megacryst cores associated with anti-correlated fractionation of Fe-Mg isotopes indicate that these elements have been rehomogenized by diffusion at high temperature. We present a 1-D model of simultaneous diffusion and crystal growth that reproduces the observed element and isotope profiles. The simulation results suggest that the cooling rate during megacryst core crystallization was slow (43 ± 21 °C/year), and consistent with pooling in a deep crustal magma chamber. The megacryst rims then crystallized 1–2 orders of magnitude faster during magma transport toward the shallower site of final emplacement. Megacryst cores had a forsterite content 3.2 ± 1.5 mol% higher than their current composition and some were in equilibrium with the whole-rock composition of NWA 1068 (Fo 80 ± 1.5). NWA 1068 composition is thus close to a primary melt (i.e. in equilibrium with the mantle) from which other enriched shergottites derived.

Keywords: Diffusion; Kinetic fractionation; Isotopic fractionation; Xenocrysts; Phenocrysts; Antecrysts; Magma ascent rates; Geospeedometry; Residence times; Martian magmatism; Fe-Mg equilibrium; Cooling rates

1. INTRODUCTION

Martian meteorites are the only rock samples available from Mars. Together with data obtained from spacecraft observations and rover missions, they hold key information on the formation and evolution of the planet. Shergottites,

* Corresponding author.
E-mail address: collinet@mit.edu (M. Collinet).

http://dx.doi.org/10.1016/j.gca.2017.03.029
0016-7037/

which are basalts or gabbros, are the most common type of martian meteorites. Among shergottites, the olivine-phyric group (Goodrich, 2002) is the most primitive, and some samples are arguably representative of liquids produced by partial melting of the mantle and not significantly affected by fractional crystallization or assimilation (Musselwhite et al., 2006; Basu Sarbadhikari et al., 2009; Peslier et al., 2010; Gross et al., 2011). These samples record magmatic processes that occurred over a large range of pressure and provide constraints on the depth and composition of their mantle sources and the shallower conditions of crystallization. Some olivine-phyric shergottites are strongly (e.g. Zipfel et al., 2000; Shirai and Ebihara, 2004; Aoudjehane et al., 2012) or moderately (Filiberto et al., 2012; Gross et al., 2013) depleted in light rare earth elements (LREE) relative to heavy rare earth elements (HREE). Other shergottites are not depleted in LREE and are characterized by higher initial $^{87}Sr/^{86}Sr$ and lower initial $\varepsilon^{143}Nd$. Shergottites from this last group are referred to as "enriched" (e.g. Barrat et al., 2002; Basu Sarbadhikari et al., 2009; Peslier et al., 2010). Shergottites have been the subject of continuous discussions (see the review by Jones, 2015) concerning their crystallization age (Bouvier et al., 2009; Moser et al., 2013), the origin of the enriched source (Debaille et al., 2008; Peters et al., 2015) and how they relate to other martian rocks (Schmidt and McCoy, 2010; Filiberto and Dasgupta, 2011). The detailed crystallization history of olivine-phyric shergottites has remained elusive due to the controversial origin of the olivine megacrysts 0.3–3 mm in diameter. These megacrysts are either interpreted as xenocrysts added to a basaltic melt (Barrat et al., 2002; Herd, 2006; Shearer et al., 2006; Filiberto et al., 2010) or phenocrysts that potentially accumulated in the magma (Filiberto et al., 2010; Balta et al., 2013, 2015; Shearer et al., 2013).

Iron and magnesium zoning profiles across olivine crystals have been used to constrain the cooling rates of terrestrial magmas (Costa and Chakraborty, 2004; Costa and Dungan, 2005; Costa et al., 2008) based on the assumption that chemical zoning mainly results from diffusion. For shergottites, it is sometimes assumed that olivine zoning results purely from rapid crystal growth in an evolving liquid. In such cases, the Fe-Mg zoning is used to reconstruct the order of appearance of different pyroxenes (orthopyroxene, pigeonite and augite) relative to olivine (Peslier et al., 2010; Gross et al., 2013). Finally, other authors modeled the combined effect of crystal growth and diffusion to constrain the cooling rates of shergottites (Mikouchi et al., 2001; Miyamoto et al., 2010). However, diffusion, crystallization or a combination of both, usually lead to non-unique profiles of Fe-Mg in olivine (see Section 4.3.1). As the origin of olivine megacrysts in shergottites is controversial, constraining the cooling rate or the crystallization sequence from the forsterite content (Fo; equivalent to $Mg\# = [Mg/(Mg + Fe^{2+})] \times 100$ with concentrations expressed in mol.%) of olivine crystals alone remains speculative.

In this work, we study zoning in olivine megacrysts of Northwest Africa (NWA) 1068. This olivine-phyric shergottite, together with Larkman Nunatak (LAR) 06319, is one of the few picritic basalts from the enriched group and, presumably, the closest in composition to a primary melt. The composition of olivine in NWA 1068 was first measured by Barrat et al. (2002) who performed individual electron microprobe (EMP) analyses and profiles in selected megacrysts and in groundmass crystals. They reported a compositional range from Fo_{42} to Fo_{72}. Herd (2006) later measured olivine crystals reaching Fo_{74} and Shearer et al. (2008) reported a composition of Fo_{75} in NWA 1110, a meteorite paired with NWA 1068. In the Earth's mantle, olivine is typically close to Fo_{90}. The martian mantle is richer in FeO (Dreibus and Wanke, 1985; Taylor, 2013) and the composition of mantle olivine should be in the range Fo_{75}–Fo_{85} (Fo_{85} corresponds to the source of "depleted" shergottites; Musselwhite et al., 2006). Olivine megacrysts in NWA 1068 (Fo 72–77) are at the lower end of this range and thus represent ideal witnesses of the deep structure and plumbing systems of a recent (185 ± 11 Ma; Shih et al., 2003) volcanic system on Mars.

In addition to element profiles, we measured the first Fe-Mg isotope profiles in shergottites to further constrain the origin and cooling history of olivine megacrysts. Recent data on Fe and Mg isotopes in olivine have revealed that diffusive isotope fractionation can exceed equilibrium isotope fractionation at magmatic temperatures (>1000 °C) by an order of magnitude (Dauphas et al., 2010; Teng et al., 2011; Weyer and Seitz, 2012; Sio et al., 2013; Oeser et al., 2015; Sio and Dauphas, 2016). Accordingly, Fe-Mg element zoning in olivine when coupled with Fe-Mg isotopic zoning allows distinguishing between chemical zoning produced by crystal growth and diffusion and to constrain cooling rates more reliably (Teng et al., 2011; Sio et al., 2013; Oeser et al., 2015; Richter et al., 2016; Sio and Dauphas, 2016).

Therefore, by studying simultaneously major and trace element contents and Fe-Mg isotope fractionation, we can observe the effect of both diffusion and crystal growth on the composition of NWA 1068 olivine megacrysts. We then model isotope and element profiles to place quantitative constraints on the crystallization history of NWA 1068 and other related enriched shergottites. In particular, we provide estimates on both the residence time of NWA 1068 parental melt in its magma chamber and the cooling rate during magma ascent and crystallization of the groundmass.

2. ANALYTICAL METHODS

Olivine megacrysts were analyzed from 2 thin sections of NWA 1068 with surface areas of 3.5 cm^2 and 0.8 cm^2. We refer to those sections as A and B, respectively. The major (Fe, Mg, Si) and minor/trace (Ca, Mn, Cr, Ti, P, Ni) elements were first measured by wavelength dispersive spectrometry (WDS) with two Cameca SX100 EMP at the "Laboratoire Magmas et Volcans" (LMV) in Clermont-Ferrand and at the Leibniz Universität Hanover (LUH). A beam current of 15 nA and a voltage of 15 kV were used for major elements. The current intensity and counting time were increased to 100 nA and 300 s (as opposed to 20 s) for trace elements. Major element maps of olivine crystals in

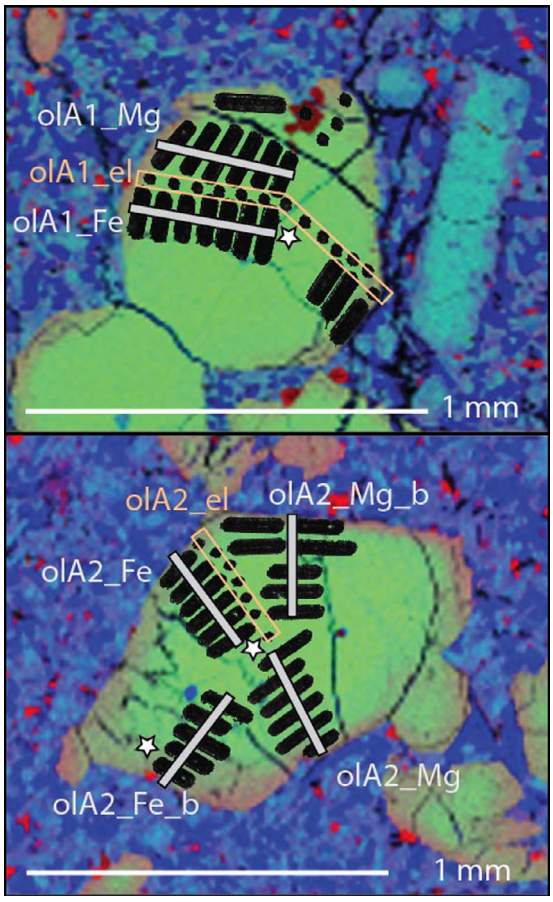

Fig. 1. Element maps of olivine A1 and A2 showing the position of LA-ICP-MS analyses. Element profiles are in orange and isotope profiles in light gray. The stars represent the EBSD analyses. RGB image with Fe in red, Mg in green and Ca in blue. (For interpretation of the references to color in this figure legend, the reader is referred to the web version of this article.)

section A (Fig. 1) were also acquired at LMV with a current of 100 nA, a 20 kV voltage (instead of 15 kV), a counting time of 40 ms, and a step of 4 μm.

Additional trace elements (V, Co, Sc, Ni, Cu, Zn and Cr) were measured by femtosecond-laser ablation (fs-LA) of the sample with a Spectra-Physics Solstice system (see Oeser et al., 2014; Lazarov and Horn, 2015 for details) connected to a fast scanning sector field ICP-MS (ThermoScientific Element XR®) at the Institute of Mineralogy, LUH. Sample ablation was performed by spot analyses with a beam diameter of 40 μm and a step width of 50 μm on average (Fig. 1). Laser repetition rate was 8–10 Hz. Each analysis started with a 30 s background acquisition, followed by an ablation interval of 40–60 s. External calibration of the acquired data was performed using the USGS reference glasses BCR-2G and BIR-1G with the preferred values reported in the GeoReM database (Jochum et al., 2005). ^{29}Si was used for internal standardization. Data reduction was performed with the Lotus-based spreadsheet program LAMTRACE (Jackson, 2008), which also automatically calculates the lower limit of detection (LLD) for each analysis using the algorithm developed by Longerich et al. (1996).

Fe and Mg isotope ratios were measured *in situ* using the same laser ablation system but connected to a ThermoFinnigan Neptune multicollector ICP-MS (MC-ICP-MS) operated in a high mass resolution mode (Weyer and Schwieters, 2003) with sample-standard bracketing following the exact procedure described in Oeser et al. (2014, 2015). Analyzing simultaneously the ^{60}Ni/^{58}Ni ratio of a Ni standard solution (NIST SRM 986) with the ablation aerosol allowed to monitor the instrumental mass bias for Fe isotopes (Poitrasson and Freydier, 2005). Using this technique, the long-term reproducibility has been shown to be better than 0.13‰ for both δ^{56}Fe and δ^{26}Mg. The within-session reproducibility, which is more appropriate for defining the uncertainties of the measured δ-values for a single isotope profile, is better than 0.10‰ (2 SD), based on replicate analyses of silicate reference glasses (Oeser et al., 2014). Ablation of olivine crystals was performed along lines of 150–200 μm in length parallel to the crystal rim with a laser spot size of ~40 μm (Fig. 1). Bracketing standards were the silicate reference glasses BHVO-2G and GOR132-G for Mg isotope analyses and BCR-2G for Fe isotope analyses. As the Fe and Mg isotopic compositions of these reference materials relative to IRMM-14 and DSM-3 are known (Oeser et al., 2014), we report isotope measurements as δ^{56}Fe and δ^{26}Mg relative to IRMM-14 and DSM-3, respectively (Eqs. (1) and (2)).

$$\delta^{56}\mathrm{Fe} = \left[\frac{^{56}\mathrm{Fe}_{\mathrm{sample}}/^{54}\mathrm{Fe}_{\mathrm{sample}}}{^{56}\mathrm{Fe}_{\mathrm{IRMM-14}}/^{54}\mathrm{Fe}_{\mathrm{IRMM-14}}} - 1\right] \times 1000 \quad (1)$$

$$\delta^{26}\mathrm{Mg} = \left[\frac{^{26}\mathrm{Mg}_{\mathrm{sample}}/^{24}\mathrm{Mg}_{\mathrm{sample}}}{^{26}\mathrm{Mg}_{\mathrm{DSM-3}}/^{24}\mathrm{Fe}_{\mathrm{DSM-3}}} - 1\right] \times 1000 \quad (2)$$

As Fe-Mg diffusion in olivine is anisotropic (Buening and Buseck, 1973; Dohmen et al., 2007), knowledge of the crystallographic orientation is necessary to constrain the Fe-Mg diffusivity. We obtained the crystal lattice orientation by electron backscatter diffraction (EBSD) measurements carried out at the Ruhr University Bochum (RUB) with a SEM Zeiss LEO 1530 Gemini Field Emission at an acceleration voltage of 20 kV, a working distance of 25 mm, and a Nordlys EBSD detector tilted by 70°.

3. RESULTS

3.1. Olivine major element compositions

In sections A and B, we observed three megacrysts with core compositions in the range of Fo_{74-75} and one glomerocryst composed of four olivine megacrysts, the largest of which has a composition of Fo_{77} (Fig. 2). Fo_{77} is the most Mg-rich olivine composition documented for NWA 1068 and paired meteorites. A few megacrysts have core compositions as low as Fo_{70} but crystal cores are usually in the range Fo_{70-74} (Figs. 3 and 4). There appears to be a continuous spectrum of core compositions from Fo_{70} to Fo_{77} rather than different populations of megacrysts. The Fo profiles of megacryst cores are relatively flat and suggest that the variability in Fo does not primarily result from a

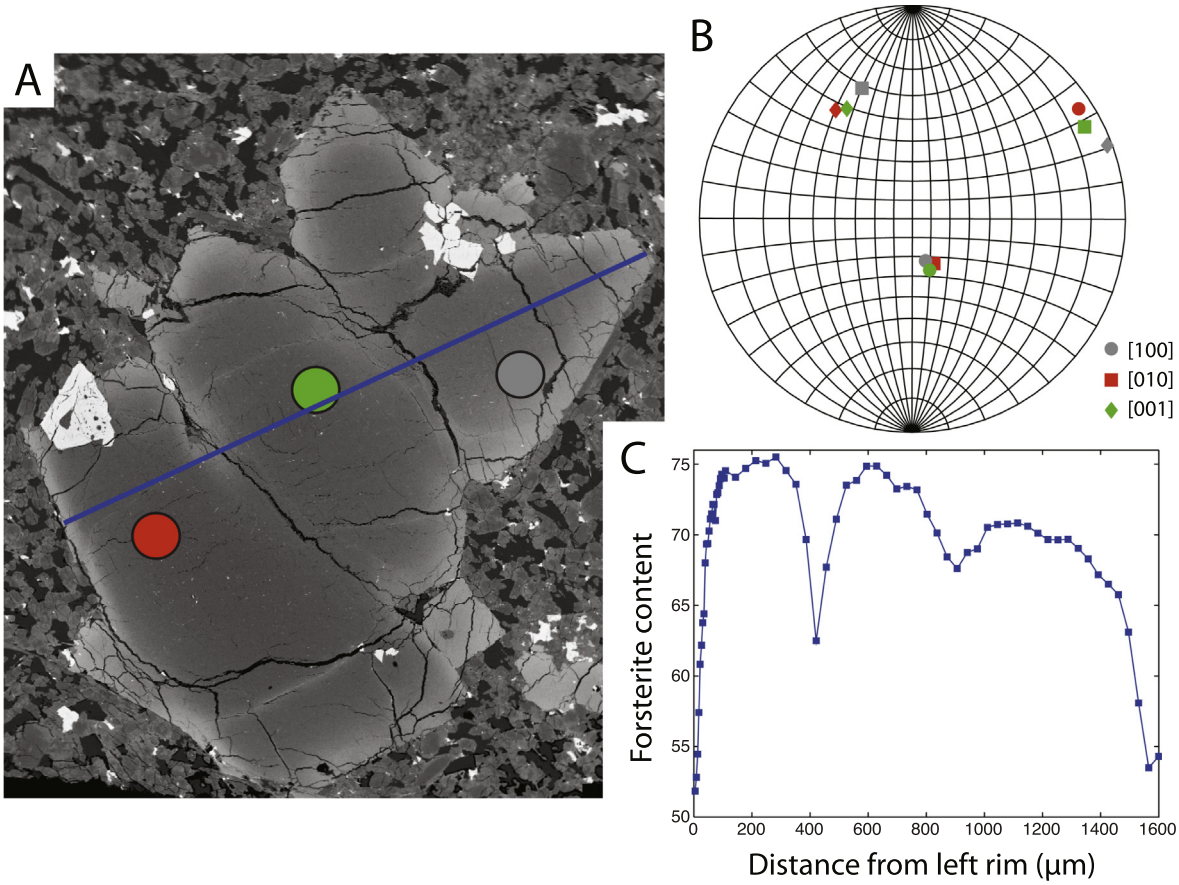

Fig. 2. Glomerocryst of olivine B4. [A] Back scattered image with the position of EBSD analyses (colored circles) and one EMP profile through the crystal (blue line). [B] Stereographic projection of the crystallographic orientation for each of the 3 crystals in [A] (colored circles). Crystals red and green are twinned on their face (0 0 1) and crystals green and gray are twinned on their face (1 0 0). [C] Forsterite profile across the glomerocryst (blue line in A). (For interpretation of the references to color in this figure legend, the reader is referred to the web version of this article.)

thin section cutting effect. Megacryst rims, usually 100–200 µm thick, show a steep zoning characterized by an outward decrease of the forsterite content down to $Fo_{57\text{-}47}$. The composition of the outer rim at the interface with the groundmass slightly varies from one megacryst to another (Fig. 3). Some forsterite profiles in the rim of megacrysts appear to be slightly "concave up" (e.g. B1, B2) while others are not (e.g. A1). Zoning is preserved within the glomerocryst and the Fo content drops significantly between the cores of adjacent twinned crystals (Fig. 2). Short-wavelength oscillatory zoning has been recently observed in some nakhlites and attributed to crystal growth processes (Jambon et al., 2016). No oscillatory zoning was found in the olivine megacrysts from NWA 1068 despite an extensive search.

3.2. Composition in minor and trace elements

The outer 100–200 µm of the rims with strong Fe-Mg zoning are also zoned for minor element concentrations. MnO increases outward from ~0.5 to ~0.75 wt.%, Ni decreases from ~700 ppm to ~400 ppm and Cr decreases from ~600–800 ppm to ~200 ppm (Fig. 3). Occasionally, Cr contents as high as 1200 ppm were measured by LA-ICP-MS in olivine cores but they likely result from the ablation of micrometric chromite crystals, which are abundant in NWA 1068 olivine megacryts (Barrat et al., 2002; Shearer et al., 2008). Similarly, V contents seem to decrease from core (~20 ppm) to rim (~12 ppm) and outlier analyses up to 50 ppm are interpreted as resulting from contamination by spinel (Table 1). Zn appears to increase from core to rim but also varies significantly between megacrysts. Sc slightly increases outward from ~6 ppm to 9–10 ppm. P contents vary between 30 and 1200 ppm but the P-zoning was not studied in detail and we refer to Shearer et al. (2013) who highlighted a complex oscillatory P-zoning. CaO contents stay relatively homogeneous throughout megacrysts (0.2–0.25 wt.%) with some excursions toward much higher CaO contents (up to 1 wt.%). Those higher CaO values result from the presence of Ca-rich carbonates precipitated within microcracks in the hot desert environment in which NWA 1068 was collected. The typical 40 µm spot-size used for LA-ICP-MS analyses makes some contamination by carbonates unavoidable. Unlike most trace elements, Ti is only zoned in the outermost 50 ± 10 µm of the megacrysts where the Ti content suddenly

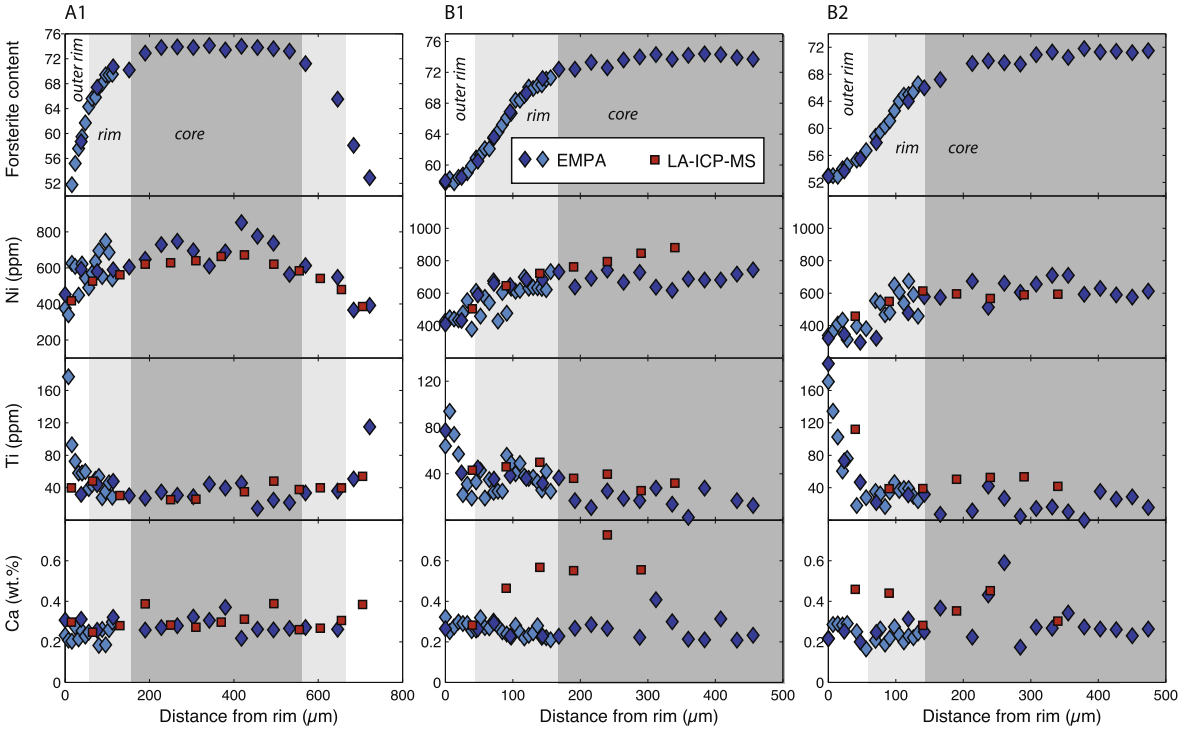

Fig. 3. Chemical profiles of major (forsterite content) and minor elements in olivines A1, B1 and B2 from EMP and LA-ICP-MS measurements. The outer rim is defined by the sharp increase in Ti and the rim is defined as the part of the crystal characterized by a steep Fo profile.

rises from ~30 ppm in core to 150–300 ppm at the megacryst-groundmass interface. Both EMP and LA-ICP-MS analyses are consistent with a Ti content of ~30–40 ppm in megacryst cores (Fig. 3), less than half of what was measured by Shearer et al. (2013) in NWA 1183. The concentrations of other trace and minor elements are consistent with previous analyses performed on NWA 1110/1183 that are both paired with NWA 1068 (Shearer et al., 2008, 2013).

3.3. Fe and Mg isotopic composition

Megacryst cores are homogeneous in isotopic compositions within analytical uncertainty and variations only appear in the ~100 μm rims of the megacrysts (Fig. 4). The Mg isotope ratios are consistent in all the megacryst cores analyzed and vary in a narrow range of 0.0 to +0.2‰ in $\delta^{26}Mg_{DSM\text{-}3}$. The Fe isotope ratios of megacryst cores, while homogeneous, are more variable ($\delta^{56}Fe_{IRMM\text{-}14}$ of −0.6 to −1.0‰) from one crystal to another. Fe and Mg isotope ratios in olivine megacryst cores are significantly fractionated relative to the bulk isotopic composition of martian meteorites. The $\delta^{56}Fe$ of virtually all the martian meteorites analyzed are identical and unfractionated relative to the standard with $\delta^{56}Fe_{IRMM14}$ of 0 ± 0.05 (Poitrasson et al., 2004; Weyer et al., 2005; Anand et al., 2006; Wang et al., 2012; Sossi et al., 2016). Early studies of Mg isotope ratios by Norman et al. (2006), Wiechert and Halliday (2007) and Chakrabarti and Jacobsen (2010) observed a large range of $\delta^{26}Mg_{DSM\text{-}3}$ (−0.1 to −0.57‰) for martian meteorites. The light measurements (−0.57‰) of Chakrabarti and Jacobsen (2010) have been shown to result from analytical artifacts (Teng et al., 2015). A recent and more exhaustive study (Magna et al., 2017) shows that 31 martian meteorites have bulk $\delta^{26}Mg_{DSM\text{-}3}$ ranging between −0.11 and −0.32‰ and that all olivine-bearing samples have a $\delta^{26}Mg_{DSM\text{-}3}$ of -0.27 ± 0.04‰. As the analysis of Fe-Mg isotopes by fs-LA-MC-ICP-MS appears to be largely matrix-independent (Steinhoefel et al., 2009; Oeser et al., 2014), we also performed two raster-mode measurements in the groundmass of NWA 1068. We obtained a $\delta^{56}Fe$ (relative to IRMM-14) of −0.03‰ and a $\delta^{26}Mg$ of −0.41‰. The $\delta^{56}Fe$ of NWA 1068 groundmass is fully consistent with the martian average of the literature. The $\delta^{26}Mg$ of the groundmass is also consistent, within the ±0.13‰ analytical uncertainty, to the recent average $\delta^{26}Mg$ of olivine-bearing martian meteorites (Magna et al., 2017). It is however possible that the groundmass of NWA 1068 is slightly lighter (−0.4‰) than this average composition. Heavier olivine cores (0.0–0.2‰) and a lighter groundmass (−0.4‰) could result in a bulk value closer to the average value of -0.27 ± 0.04‰.

Olivine megacryst cores have heavier Mg isotopes and lighter Fe isotopes relative to all bulk martian meteorites and to the groundmass of NWA 1068. Their $\delta^{26}Mg$ are higher by 0.3–0.5‰ and their $\delta^{56}Fe$ are lower by 0.6–1.0‰ (Fig. 4). On the contrary, the rims of olivine megacrysts converge toward the average isotopic compositions of the literature (martian meteorites) and NWA 1068 groundmass ($\delta^{26}Mg$ ~−0.4 or −0.25‰ and $\delta^{56}Fe$

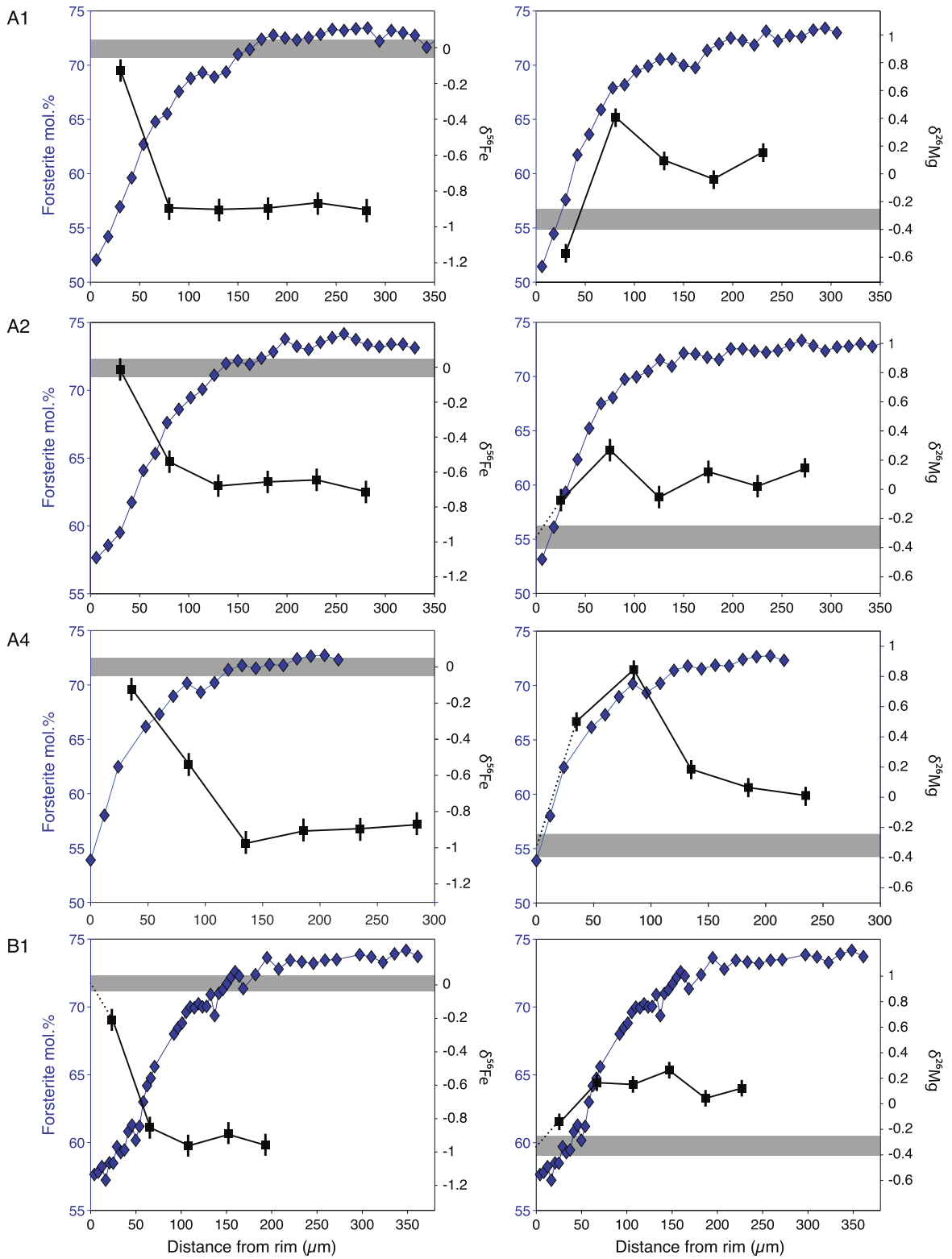

Fig. 4. Forsterite and isotope profiles in olivine A1, A2, B1, B2, B5 and B7, all the megacrysts for which isotope measurements are available. Error bars are 2 standard deviations (0.10‰). The gray horizontal bar represents the average isotopic composition for martian rocks from the literature and *in-situ* analysis of NWA 1068 groundmass (see text for detail).

~0.0‰). The Mg isotope profiles of some olivine megacrysts are more complex and are characterized by a spike of heavier isotopes in the intermediate rim (50–100 μm from the outer rim). This spike typically reaches higher values of δ^{26}Mg (0.3–0.4‰) than those observed for megacryst cores and can reach a δ^{26}Mg of 0.9‰ (A4 and B7, Fig. 4).

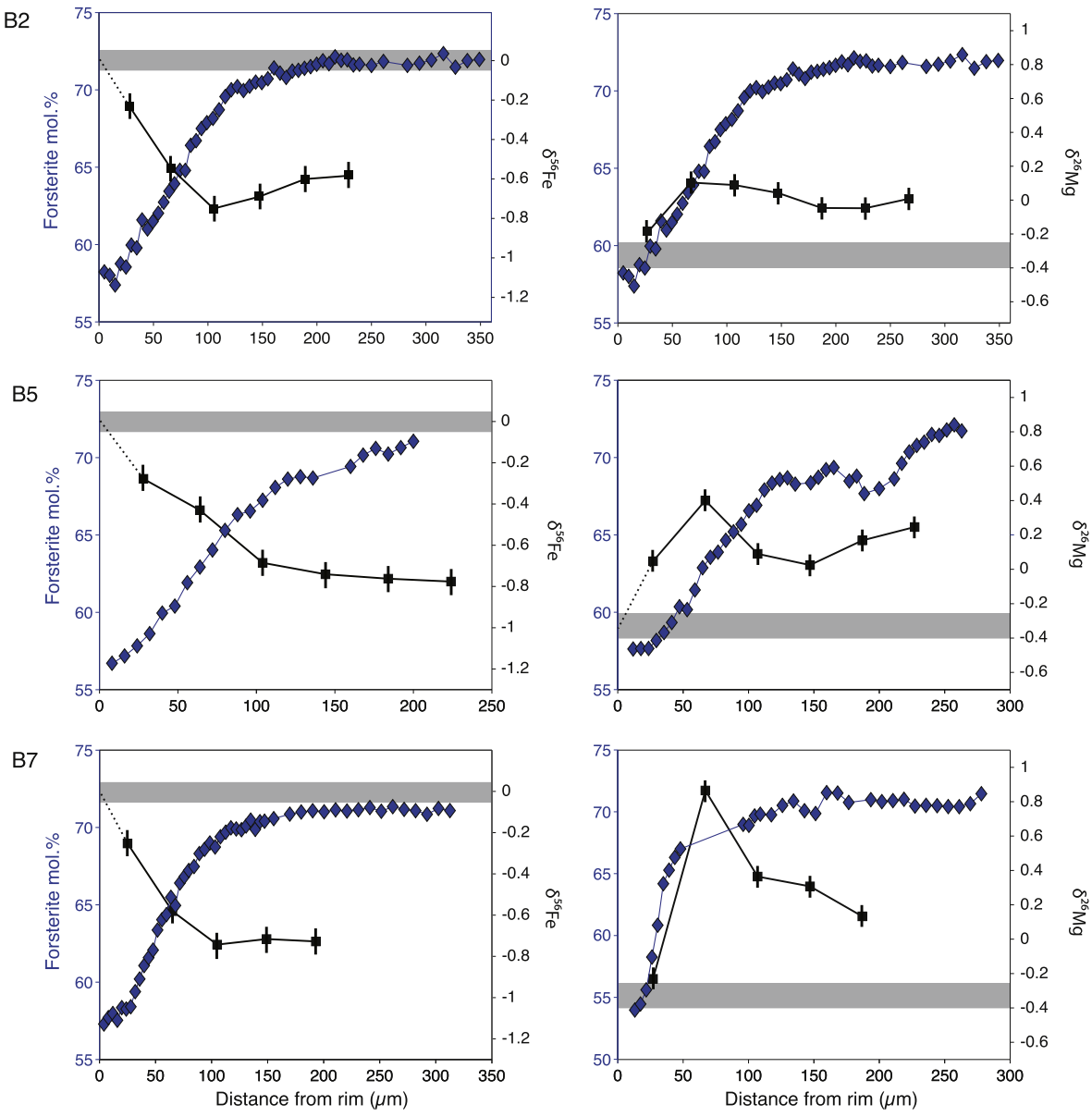

Fig 4. *(continued)*

4. DISCUSSION

4.1. Nomenclature and origin of olivine megacrysts in shergottites

The origin of olivine megacrysts in olivine-phyric shergottites is controversial as reflected by the complex and sometimes inconsistent nomenclature used in the literature. Numerous authors used the term xenocryst to refer to the megacrysts (McSween and Jarosewich, 1983; Wadhwa et al., 2001; Barrat et al., 2002; Goodrich, 2003; Koizumi et al., 2004; Herd, 2006; Shearer et al., 2006; Filiberto et al., 2010) while others preferred the term phenocryst (Mikouchi et al., 2001; Taylor et al., 2002; Koizumi et al., 2004; Musselwhite et al., 2006; Shearer et al., 2008, 2013; Usui et al., 2008; Basu Sarbadhikari et al., 2009, 2011; Peslier et al., 2010; Filiberto and Dasgupta, 2011; Gross et al., 2011, 2013; Balta et al., 2013, 2015; Liu et al., 2016). Xenocrysts are generally defined as disequilibrium crystals with no genetic relationship to the magma. Phenocrysts are equilibrium crystals that formed within the magma and reached a large size as a consequence of low nucleation rates. In the recent literature, the term phenocryst is generally preferred due to the fact that the trace element contents (Ni, Co, Y) of megacryst cores (Shearer et al., 2008), the composition in major elements and REE of melt inclusions (Shearer et al., 2008; Basu Sarbadhikari et al., 2009, 2011), and the isotopic systematics (Shafer et al., 2010) are all consistent with a common origin of the groundmass and olivine megacrysts. However, megacryst cores would have formed during an early stage of crystallization and would have been later mobilized by the melt

Table 1
Composition of trace elements in olivine megacrysts (ppm). Core compositions are the average of 3–5 analyses and σ is the standard deviation on those analyses. Rim compositions represent a single analysis.

		Core	σ	Rim
Sc	olA1	6.72	0.36	8.2
	olA2	5.74	0.3	8.7
	olA3	7	0.9	7.9
	olA4	7.5	0.3	9.7
	olB1	6.1	0.3	8.9
	olB2	8.4	1.4	9.2
	olB3	6.9	0.2	7.1
V	olA1	18.1	3.2	14.6
	olA2	17.5	2.1	11.6
	olA3	19.1	3.5	8.2
	olA4	23	2.4	16.5
	olB1	23	1.9	20.4
	olB2	17	2.1	13.9
	olB3	23.5	4.2	9.6
Cr	olA1	630	122	283
	olA2	756	103	274
	olA3	771	147	152
	olA4	756	153	251
	olB1	1025	240	448
	olB2	986	220	261
	olB3	1025	304	198
Co	olA1	101	6	118
	olA2	85.7	2	91
	olA3	94	4.5	91.7
	olA4	96.5	0.3	98.1
	olB1	112	0.7	115
	olB2	104	3	107
	olB3	100	1	97
Ni	olA1	633	30	418
	olA2	606	15	379
	olA3	611	89	345
	olA4	728	39	446
	olB1	1085	75	659
	olB2	647	14	512
	olB3	621	13	434
Cu	olA1	10.8	0.6	6.7
	olA2	10.3	0.7	6.4
	olA3	10.7	0.8	10.4
	olA4	11.3	1	10.2
	olB1	11.75	0.2	9
	olB2	9.7	0.5	7.3
	olB3	8.3	0.5	5.7
Zn	olA1	88	22	104
	olA2	69	3	95
	olA3	93	16	98
	olA4	151	6	146
	olB1	68.5	3	96
	olB2	88	11.4	88
	olB3	70	7	76

that crystallized the groundmass. Several authors have suggested that when the magma crystallized near the surface, it contained the megacrysts from more than one liquid aliquot such that most olivine-phyric shergottites contain >10 wt.% of "accumulated phenocrysts" also referred to as "antecrysts". This line of reasoning is based on two main arguments: (1) most bulk rock compositions of olivine-phyric shergottites are too rich in Mg compared to a liquid in equilibrium with megacryst cores (e.g. Filiberto and Dasgupta, 2011); (2) the crystal size distribution (CSD; Marsh, 1988) of olivine is kinked around 1.5 mm due to an excess of large crystals (e.g. Basu Sarbadhikari et al., 2009; Ennis and McSween, 2014; Balta et al., 2015).

Different authors have slightly different definitions of phenocrysts, antecrysts, accumulated phenocrysts and xenocrysts. Large crystals of different origins can also locally coexist in a single rock. Therefore, the crystallization history of the large olivine crystals relative to the groundmass cannot be summarized by a single term. As we describe the crystallization history of the large olivine crystals in NWA 1068, we will continue to refer to them as olivine megacrysts, a term that is free of any petrogenetic connotation.

4.2. Origin of the chemical zoning in olivine megacrysts of NWA 1068

Olivine megacrysts in NWA 1068 were first interpreted as xenocrysts derived from disrupted cumulates, possibly co-genetic with the groundmass (which some authors would call "antecrysts"), but occasionally showing disequilibrium textures (Fig. 7 from Barrat et al., 2002). The forsterite content of the cores was described as flat (at $\sim Fo_{72}$) and the zoning of the rim as resulting chiefly from diffusion driven by contact with the Fe-rich melt that later formed the groundmass. Shearer et al. (2008, 2013) confirmed that the megacrysts were genetically related to the groundmass by analyzing minor elements in olivine (P, Ni, Co, Y) and in olivine melt inclusions (REE). However, Filiberto et al. (2010) and Filiberto and Dasgupta (2011) argued that olivine megacrysts were partly accumulated based on the Mg# of the bulk-rock. Herd (2006) showed that the olivine megacrysts in NWA 1068 also crystallized at different redox conditions (FMQ-2.5) than the groundmass (FMQ + 0.5). While this observation was first inferred to point toward a "xenocrystic origin" of megacrysts, it was later shown that it is also consistent with closed system crystallization and result from the incompatible behavior of Fe^{3+} (Peslier et al., 2010) and/or the degassing of volatile elements (Balta et al., 2013; Shearer et al., 2013).

Despite the increased understanding of the crystallization conditions of NWA 1068, the origin of the Fe-Mg zoning in megacrysts and the timescale of crystallization remain ambiguous. The initial interpretation of forsterite profiles by Barrat et al. (2002) and Mikouchi and Miyamoto (2002) was that only the olivine rims were affected by diffusion as megacrysts cores are nearly homogeneous in composition. When an olivine crystal is placed in a melt that is enriched in Fe compared to the liquid from which the olivine crystallized, Fe-Mg interdiffusion will progressively bring the olivine toward a more Fe-rich equilibrium composition (Fig. 5). As heavy isotopes diffuse slightly slower than the light ones (Jambon, 1980; Richter et al., 1999), the inward replacement of Mg by Fe (decrease in Fo content) also enriches the olivine crystals in ^{26}Mg

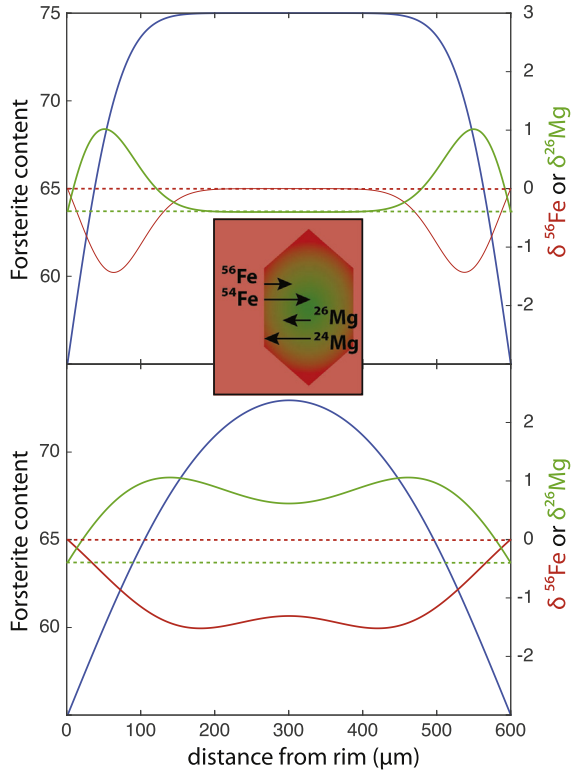

Fig. 5. Evolution of Fo content and Fe-Mg isotope fractionation during simple diffusion in olivine (see Section 4.3.1 for model description). Isotope fractionation affects the rim first and the core remains chemically homogeneous. When isotope fractionation reaches the core, the Fo profile is curved.

relative to ^{24}Mg and depletes them in ^{56}Fe relative to ^{54}Fe (Teng et al., 2011; Sio et al., 2013; Oeser et al., 2015). Diffusion first lowers the Fo content of the rims while leaving the core unaffected. No isotope fractionation is observed in the core at this stage (Fig 5; Oeser et al., 2015; Richter et al., 2016). As the olivine crystal continues to equilibrate, Fe-Mg isotope fractionation progressively reaches the core. The Fo profile of the core is no longer flat but forms a smooth (bell-like) curve (Fig. 5; Sio et al., 2013). In NWA 1068, the cores of olivine megacrysts have relatively flat Fo and Ni profiles and only the rims display a strong zoning (rims and outer rims in Fig. 3). However, the cores of megacrysts are also characterized by the anti-correlated isotope fractionation that is characteristic of diffusion (Fig. 4). Those combined observations are incompatible with diffusion alone accounting for the isotope and element profiles of NWA 1068 megacrysts.

Diffusion of Fe and Mg in olivine is anisotropic and 4–8 times faster along the crystallographic *c*-axis (Dohmen et al., 2007). Crystallographic orientations obtained from EBSD measurement were used to calculate the diffusivity of Fe-Mg at a fixed temperature, pressure, redox condition and starting olivine composition (Dohmen et al., 2007; Dohmen and Chakraborty, 2007; also see Section 4.3.1). We find no simple correlation between the diffusivity along each Fo profile and the chemical gradient of the rims (Fig. 6). If the Fo zoning resulted purely from diffusion, the chemical gradient would be expected to be weaker for directions at low angle of the *c*-axis (larger diffusivities). Yet, there are clear signs that olivine megacrysts were affected by diffusion. The presence of Fe-Mg anti-correlated isotope fractionation in the core indicates that diffusion influenced the composition of megacryst cores. In addition, oscillatory growth zoning (Jambon et al., 2016) is only preserved by the slowest diffusing element (P; Shearer et al., 2013) and was erased by diffusion for other, faster diffusing, elements (Fig. 3).

Important evidence suggests that the strong zoning of the megacryst rims actually results partly from crystal growth in a melt of evolving composition. Forsterite zoning is preserved between the crystals of the olivine glomerocryst (Fig. 2). This indicates that olivine of Fe-rich composition was crystallizing when the crystals grew and got attached to each other. The small olivine crystals within the groundmass have the same composition as the megacryst outer rims. The liquid from which the groundmass crystallized was thus saturated in olivine and both the small crystals and megacryst rims formed simultaneously. Shearer et al. (2013) interpret complex P-maps of NWA 1183 megacrysts as highlighting different stages of crystal growth. The last one would have formed the outer ~50 μm of the olivine megacrysts. We postulate that the sharp Ti enrichment in the outermost 40–60 μm of megacryst rims in NWA 1068 (see outer rims, Fig. 3) results from the same final stage of crystal growth. The sudden rise in Ti concentration could result from entrapment in the interfacial region (e.g. Watson, 1996) or from the development of a diffusive boundary layer in the silicate melt, as suggested by Shearer et al. (2013) for P. Explaining the Ti enrichment without some type of kinetic disequilibrium would require an increase in the partitioning of Ti between olivine and the melt or in the concentration of Ti in the residual melt

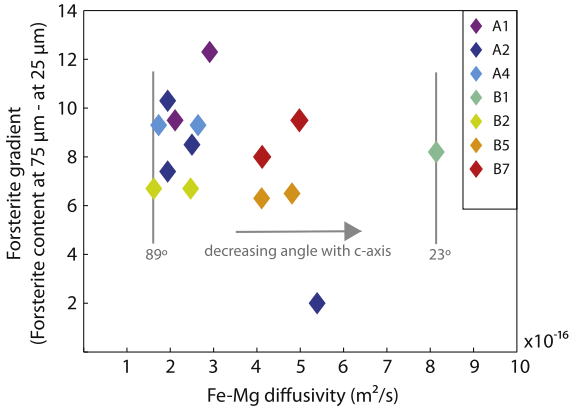

Fig. 6. Comparison between the difference in forsterite content at 75 μm and 25 μm from the megacryst rims (forsterite gradient) and the Fe-Mg diffusivity along each profile based on the crystallographic orientation. The diffusivities are calculated following Dohmen et al. (2007) and Dohmen and Chakraborty (2007) for a temperature of 1390 °C, a pressure of 1 bar, an average Fo content of 70, a fO_2 at the FMQ buffer and considering that the diffusivity is 6 times higher along the *c*-axis compared to crystallographic axes *a* and *b*.

by at least one order of magnitude. The profiles in other minor and trace elements are more similar to the Fo profiles with zoning affecting the outer 200 μm of megacrysts. Like Fe and Mg, these minor elements are mainly divalent, more compatible in olivine relative to Ti, and characterized by faster diffusivities relative to Ti^{4+} (Richter et al., 2003). We suggest that the Ti zoning preserved the initial size of a crystal overgrowth (outer rims, Fig. 3), which formed during a shallower and faster stage of crystallization.

Atoms of the same element can also move within the crystal lattice in the absence of chemical gradient. This process, known as self- or tracer-diffusion (e.g. Chakraborty et al., 1994), would erase the anti-correlated Fe-Mg isotope fractionation over time if the megacrysts were maintained at high pressure and temperature. The presence of Fe-Mg isotope fractionation in the megacryst cores of NWA 1068 indicates that, while preceding the crystallization of the groundmass, the megacryst cores are not derived from the mantle or ancient crustal cumulates produced in an older magmatic system. Instead, as suggested by the composition of minor elements (Shearer et al., 2008, 2013), olivine megacrysts must be co-genetic with the groundmass.

In summary, olivine megacrysts in NWA 1068 were formed by the crystallization of a melt genetically related to the melt that formed the groundmass. The isotope fractionation of megacryst cores indicates that their composition was progressively enriched in Fe by diffusion and that they likely grew slowly in a melt of evolving composition. The 50 μm outer rims crystallized faster than the rest of the megacryst. The Fo profiles of olivine megacrysts thus result from the simultaneous influence of crystal growth and diffusion.

4.3. Diffusion-crystallization models

In order to place quantitative constraints on the cooling rate of the different stages of NWA 1068 crystallization described in the above section and previously proposed in the literature (Filiberto et al., 2010; Shearer et al., 2013), we describe a model of simultaneous diffusion and crystal growth with variable successive cooling rates. We first illustrate how more simple models are inadequate to reproduce the complex chemical and isotope profiles of NWA 1068 olivines. Finally, we discuss the uncertainties associated with the model of combined diffusion and crystal growth.

4.3.1. Simple diffusion and crystallization models

The methods used to simulate crystal growth and diffusion are first described separately. These simple models illustrate that crystallization or diffusion alone cannot reproduce the isotope and element profiles of olivine crystals in NWA 1068. However, once combined, they constitute the framework of the model of simultaneous growth and diffusion, which provides quantitative constraints on the cooling history of NWA 1068 (Section 4.3.2).

For the simple diffusion model, we used the one-dimension diffusion equation with the diffusion coefficient (D in m^2/s) varying as a function of the mole fraction of FeO or MgO (C) in olivine and the position (x) along the profile:

$$\frac{\partial C(x,t)}{\partial t} = \frac{\partial D}{\partial x}\frac{\partial C(x,t)}{\partial x} + D\frac{\partial^2 C(x,t)}{\partial x^2} \quad (3)$$

The diffusion equation was solved numerically using the finite difference method (e.g. Costa et al., 2008). The Fe-Mg diffusivity was calculated, parallel to the c-axis, using the following expression (Dohmen et al., 2007; Dohmen and Chakraborty, 2007):

$$D_{\mathrm{Fe-Mg}} = 10^{-9.21}\cdot\left(\frac{fO_2}{10^{-7}}\right)^{1/6}\cdot 10^{3(X_{\mathrm{Fe}}-0.1)} \cdot\exp\left(-\frac{201,000+(P-10^5)\cdot 7\cdot 10^{-6}}{RT}\right) \quad (4)$$

where fO_2 is the oxygen fugacity and P is the pressure (both in Pascals), T is the temperature in Kelvin and X_{Fe} is the mole fraction of fayalite.

The diffusivity of ^{56}Fe (~92% of total Fe isotopes) and ^{24}Mg (~77% of total Mg isotopes) are set equal to the Fe-Mg interdiffusion coefficient (Eq. (4)). The diffusivity of other isotopes is calculated using the following empirical formula (Richter et al., 1999) which is a modified version of Graham's law for molten oxides and crystals:

$$\frac{D_1}{D_2} = \left(\frac{M_2}{M_1}\right)^{\beta} \quad (5)$$

where D_1 and D_2 are the diffusivity and M_1 and M_2 the masses of two isotopes of the same element. The exponent β is 0.5 in a gas but is known to be smaller in olivine crystals and in the range 0.08–0.16 for Mg and 0.16–0.27 for Fe (Sio et al., 2013; Oeser et al., 2015). Results from Oeser et al. (2015) point toward the lower values and both studies are consistent with the estimated β-Fe/β-Mg ratio (≈2; Van Orman and Krawczynski, 2015). β-Mg and β-Fe were varied in a range of 0.08–0.28 and 0.12–0.32, respectively.

The initial composition of the olivine crystal is homogeneous (i.e. no chemical zoning), based on the assumption that megacrysts were fully equilibrated. To set this initial composition, the bulk composition of NWA 1068 is adjusted by subtracting or adding olivine incrementally until the bulk composition corresponds to the parental melt of the olivine of interest (e.g. Mg# = 47.1, in the case study of Fig. 7A). The parental melt of each olivine is thus assumed to vary from the NWA 1068 bulk composition by adding or subtracting an olivine component only. The parental melt is selected when it reaches equilibrium conditions (using a K_D Fe-Mg olivine-liquid of 0.35; Toplis, 2005; Filiberto and Dasgupta, 2011) with the daughter olivine (e.g. Fo 71.8, Fig. 7A). The composition of the groundmass parental melt is calculated using the same technique, by removing olivine from the bulk composition of NWA 1068 until a composition in equilibrium with megacrysts outer rims is reached. The composition of the groundmass parental melt is then used to calculate the temperature of the system as the MgO content of olivine-saturated basaltic liquids varies linearly with the temperature (e.g. Sugawara, 2000). We used a set of unpublished experiments performed at LMV in a 1-atm gas mixing furnace from the bulk composition of LAR 06319/NWA 1068 to parameterize the following linear relationship:

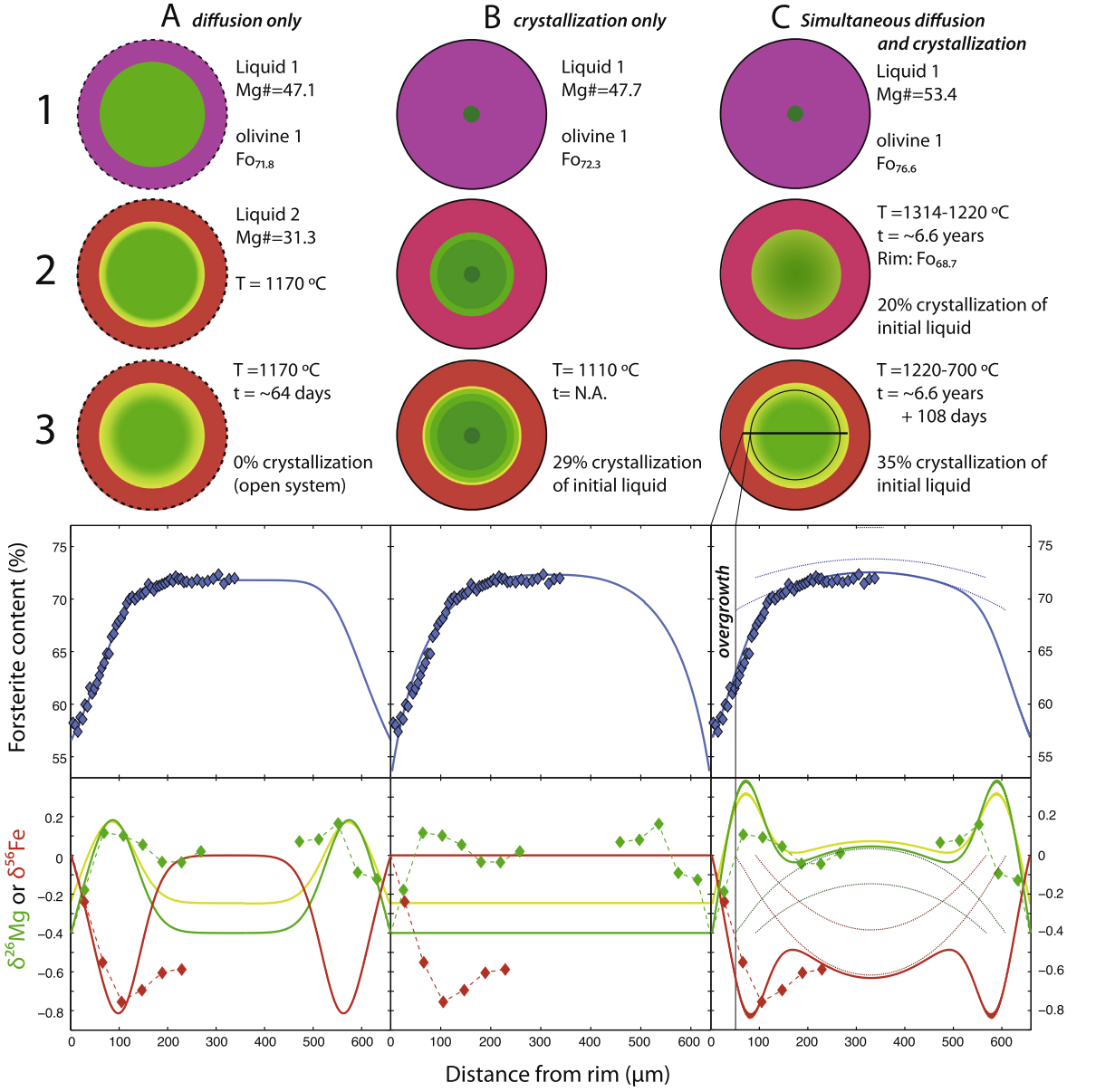

Fig. 7. Schematic representation of the three models, resulting forsterite and isotope profiles and comparison with profiles measured in olivine B2. The 2 shades of green bracket the uncertainty on the unfractionated composition of Mg isotopes. Light green: β-Mg = 0.15, initial $\delta^{26}Mg = -0.25$. Dark green: β-Mg = 0.21, initial $\delta^{26}Mg = -0.4$. [A] Simple diffusion model. [B] Simple crystallization model. [C] Model of simultaneous diffusion and crystallization. The dotted lines represent the profiles at an intermediate stage, before the outer rim (overgrowth) crystallize. The case study in C corresponds to simulation olB2_b from Tables 2 and 3. (For interpretation of the references to color in this figure legend, the reader is referred to the web version of this article.)

$$T(^{\circ}C) = MgO_{liquid}\ (wt.\%) \times 23.15 + 1022 \quad (6)$$

The experiments were conducted at fO_2 conditions 2.5 log-unit under the fayalite-magnetite-quartz (FMQ) buffer. This equation is consistent (within ±30 °C) with the results of published 1-atm experiments performed on similar bulk compositions and under similar redox conditions (Monders et al., 2007; Filiberto et al., 2008, 2010). The Fe-Mg diffusivity is then calculated using Eq. (4) and the temperature of Eq. (6). The pressure is set to 0.1 MPa and the fO_2 is set at the FMQ buffer, the crystallization conditions of NWA 1068 groundmass (Herd, 2006). The diffusion of Fe and Mg in basaltic melts is several orders of magnitude faster than Fe-Mg interdiffusion in olivine (Zhang et al., 2010). Therefore, we only model diffusion in olivine megacrysts and consider that diffusion in the melt is infinitely fast. To match the forsterite zoning of olivine megacrysts, the diffusion process has to be interrupted before the core is affected. In consequence, no isotope fractionation is generated in the core (Fig 7A), in disagreement with the strong isotope fractionation relative to the bulk shergottites measured in megacryst cores.

For the other simple model, we assume that olivine crystallization is infinitely fast and that the effect of diffusion is insignificant. The zoning in Fo content appears spontaneously by crystal growth. Olivine grows from a fixed volume of evolving liquid that is progressively depleted in MgO relative to FeO. The chosen volume of liquid (density of 2.8 g/cm^3) is converted into a mass. Like in the previous model, the composition of the initial liquid is obtained by removing incrementally olivine from NWA 1068 bulk composition until it is in equilibrium with a specific megacryst core. The starting temperature is calculated using Eq. (6). The temperature is then decreased and, at each step, the MgO content of the residual liquid is recalculated. The amount of olivine crystallized at each increment is calculated by mass balance from the amount of olivine needed to accommodate the change of MgO content of the liquid. The mass transferred from the liquid to the olivine is converted into a volume assuming an average density of 3.6 g/cm^3 for olivine. Finally, the volume is converted into the corresponding segment length and added to Fe and Mg profiles.

The crystal growth rate is controlled by the mass balance calculation but can be approximated by a simple growth law. If a constant mass of material is added to a sphere per temperature increment, the growth rate depends on to the radius of the sphere (R):

$$\frac{dR}{dt} = C\frac{1}{R^2}\frac{dT}{dt} \tag{7}$$

C scales with the mass of olivine added per increment of temperature, which depends on the initial volume of liquid. The model described here slightly deviates from Eq. (7). As the mass of residual liquid is progressively transferred to olivine, the mass of olivine necessary to accommodate the linear decrease in MgO content of the liquid (and the decrease in temperature) is ~40% smaller at the end of crystallization than at the beginning. Therefore, C is not strictly a constant but also decreases as crystallization advances. The growth law also implies that crystal growth only occurs when the temperature is decreasing, which is not necessarily the case. Undercooling, surface energy minimization and diffusion-limited transport are a few examples of processes that can induce crystal growth at constant temperature (also see Sio and Dauphas, 2016).

As the cooling rate is first assumed to be infinitely fast, diffusion is insignificant and no isotope fractionation can develop in olivine megacrysts (Fig. 7B). The equilibrium fractionation between melt and olivine is assumed to be negligible as well as potential fractionation due to crystal growth kinetics. Equilibrium fractionation of Fe isotopes can occur in the melt between Fe^{2+} and Fe^{3+} and with changes in oxygen fugacity but is expected to be negligible in a basaltic melt under reducing conditions and is thus not taken into account (Dauphas et al., 2014). Like the simple diffusion model, this model cannot reproduce the isotope profiles of NWA 1068 olivine megacrysts.

4.3.2. Simultaneous crystal growth and diffusion model

As discussed in Section 4.1 and illustrated in the above section, forsterite and isotope profiles of NWA 1068 olivine megacrysts cannot be reproduced by simple diffusion or crystal growth models. This is not a surprise considering the complex history of NWA 1068, which formed during several stages of crystallization. Diffusion and crystal growth are the two endmember processes that lead to crystal zoning in a closed system. When olivine megacrysts crystallize slowly, both processes are likely to have a significant influence on the final zoning. For this reason, both simple models described in Section 4.3.1 are combined in a crystallization and diffusion model.

The simultaneous crystallization and diffusion model is divided in three stages characterized by different cooling rates (CR). During the first stage, the temperature is decreased slowly (CR1) to allow megacryst cores to be affected by diffusion during their growth. The second stage is characterized by a much faster cooling rate and corresponds to the crystallization stage during which the groundmass and the outermost 40–60 μm rim of olivine megacrysts crystallized (CR2). The third and final stage is the final cooling of the sample after crystallization stopped and until the temperature drops below 700 °C, where diffusion becomes negligible (CR3). The cooling rate of this last stage is chosen to be equal to or greater than CR2. The fO_2, which is one of the key variables in the diffusivity equation (4), is changed from FMQ-2.5 to FMQ between stage 1 and stage 2 to account for the change of fO_2 recorded by NWA 1068 (Herd, 2006). During stages 2 and 3, the cooling rates are chosen to be sufficiently fast to preserve a sub-homogenous forsterite profile in the megacryst core but slow enough to allow diffusion to affect the outer 100–200 μm of the crystal.

The initial composition of the parental melt is calculated by adding an arbitrary olivine component to the melt in equilibrium with the olivine megacryst. Then, the initial temperature is calculated from the MgO content of this liquid (Eq. (6)). The initial volume of liquid is adjusted such that ~20% of the liquid has crystallized at the end of stage 1. This implies that all megacrysts, regardless of their size, crystallize from the same fraction of melt. An olivine fraction of 20% is close the actual modal composition of NWA 1068.

Once the model parameters are initialized, the temperature is progressively decreased following the 3 fixed cooling rates by increment of time (10 s) and the MgO content of the liquid is continuously adjusted. The fO_2 is maintained 2.5 log units under the FMQ buffer (or on the FMQ buffer for stages 2 and 3) and recalculated to reflect the change in temperature (Huebner, 1971; O'Neill, 1987):

$$\log fO_2 = 82.76 - \frac{30685.7}{T} + 0.092\frac{P-1}{T} - 10.6199 \times \ln T + 0.00484 \tag{8}$$

with fO_2 and P in bars and T in Kelvin.

The composition and amount of olivine crystallized are calculated to accommodate the change in MgO of the liquid (Eq. (6)). For each time increment, the diffusivity of each isotope along the c-axis is recalculated (Eqs. (4) and (5)) to account for the changing Fo content, temperature, and redox conditions (Eq. (8)). The volume of residual liquid between stages 1 and 2 can be decreased while keeping

the composition unchanged. Modifying the volume of residual liquid could be justified by the onset of pyroxene crystallization in the groundmass. As pyroxene and smaller olivine crystals nucleate and start to form the groundmass, they compete with the growth of megacrysts.

This model is more realistic than simple diffusion and crystal growth model and produces profiles that match the observations much better (Figs. 7C and 8, EA4). In particular, the relatively flat and fractionated isotope profiles in olivine megacrysts can now be reproduced. The cooling rate of each stage provides a duration estimate for the main crystallization steps. The model can also be used to constrain the initial composition of olivine that first crystallized from the parental melts and thus constrain the composition of the parental melt itself. The model parameters used for each simulation are listed in Table 2. Table 3 summarizes the key outputs of the model for several simulations that produced a good fit. The corresponding profiles are available in Figs. 7C and 8 and EA4.

4.3.3. Model uncertainties and limitations

The model of simultaneous crystallization and diffusion described above contains many different parameters that can be independently adjusted (Table 2). Changing several parameters simultaneously can balance the effect of each modification in such a way that the simulation outputs are very similar (Table 3). The isotope and forsterite profiles of each megacryst can thus be reproduced with slightly different parameters and each simulation does not lead to entirely unique results, especially once the analytical uncertainties are taken into account. In Tables 2 and 3, the input parameters and the results of a set of simulations that reproduce reasonably well the Fo and isotope profiles are presented for 7 different olivine megacrysts.

The parameter space that can reproduce the isotope and Fo profiles of megacryst cores is fairly limited. The cooling rate during core crystallization (CR1) can only be changed by a factor of ~5, while modifying other parameters, to maintain a strong isotope fractionation in megacryst cores. To illustrate this, we include, in Tables 2 and 3, two simulations (olB2_bf and olB2_bs) that only differ from olB2_b (Fig. 6C) by the cooling rate CR1. The cooling rate was either increased or decreased by one order of magnitude. In both cases, the isotope fractionation in the megacryst core is much lower than what was analyzed.

The main uncertainty concerns the relative timescale of rim crystallization (CR2) vs. diffusion-only cooling (CR3). For example, a faster cooling rate for the diffusion-only stage can be counterbalanced by a slower cooling rate for rim crystallization. The most conservative assumption is to keep both cooling rates equal and calculate the elapsed time between the onset of rim crystallization and the final emplacement, defined as when the temperature drops under 700 °C.

The lack of constraints on the unfractionated composition of Mg isotopes (δ^{26}Mg -0.25 or -0.4 ‰, see Section 3.3) is another source of uncertainty. However, most of this uncertainty is reported on the β and does not affect significantly other model parameters. A starting δ^{26}Mg of −0.4‰ and a β-Mg of 0.24–0.21 (dark green in Figs. 7 and 8) produce the same profiles as a δ^{26}Mg of −0.25‰ and a β-Mg of 0.17–0.15 (light green in Figs. 7 and 8). It

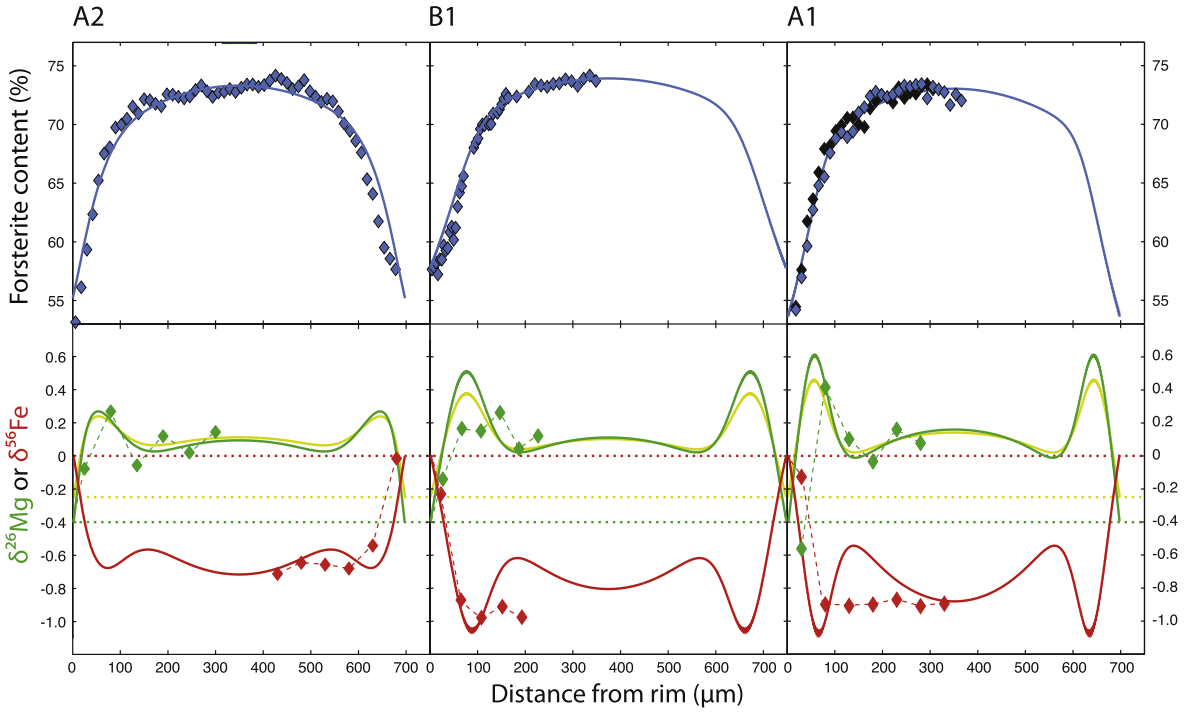

Fig. 8. Example of simulations of the simultaneous diffusion and crystallization model for three other olivine crystals (A2, B1 and A1). The simulations correspond to the rows of Tables 2 and 3 appearing in bold. The dotted lines are the unfractionated, average isotopic compositions for Mars.

Table 2
Model parameters.

	CR1 °C/s	CR2 °C/s	CR3 °C/s	β-Fe	β-Mg	∅total μm	Rim (∅/2) μm	∅sph μm	∅sph2 μm	Mg# liq1 mol.%
olA1_a	7.0E−07	6.0E−05	6.0E−05	0.3	0.25/0.17	670	37.5	1000	860	54.2
olA1_b	**8.5E−07**	**8.0E−05**	**8.0E−05**	**0.31**	**0.24/0.17**	**700**	**50**	**1000**	**940**	**54.2**
olA2_b	9.0E−07	1.5E−05	1.0E−03	0.25	0.22/0.16	700	40	1050	920	54.0
olA2_a	**1.0E−06**	**2.0E−05**	**1.0E−03**	**0.25**	**0.22/0.16**	**700**	**40**	**1050**	**920**	**53.8**
olA2_c	8.0E−07	5.0E−05	1.0E−04	0.25	0.22/0.16	690	35	1060	900	54.0
olA4_a	1.1E−06	1.2E−04	1.2E−04	0.31	0.24/0.17	570	55	770	770	56.1
olB1_a	8.0E−07	8.0E−05	8.0E−05	0.3	0.25/0.17	750	70	1060	1040	54.4
olB1_b	**7.0E−07**	**4.5E−05**	**4.5E−05**	**0.28**	**0.23/0.16**	**750**	**45**	**1100**	**1000**	**55.3**
olB2_a	9.0E−07	5.0E−05	5.0E−05	0.22	0.18/0.13	660	40	960	930	53.4
olB2_b	**7.0E−07**	**5.5E−05**	**5.5E−05**	**0.25**	**0.21/0.15**	**660**	**50**	**960**	**920**	**53.4**
olB2_bs	*7.0E−08*	*5.5E−05*	*5.5E−05*	*0.25*	*0.21/0.15*	*660*	*50*	*960*	*920*	*53.4*
olB2_bf	*7.0E−06*	*5.5E−05*	*5.5E−05*	*0.25*	*0.21/0.15*	*660*	*50*	*960*	*920*	*53.4*
olB2_c	7.0E−07	6.0E−05	6.0E−05	0.28	0.21/0.15	660	60	960	940	53.1
olB5_a	1.2E−06	6.0E−05	6.0E−05	0.29	0.25/0.17	520	50	760	760	50.9
olB5_b	9.0E−07	4.0E−05	4.0E−05	0.29	0.25/0.17	520	40	800	740	50.9
olB5_c	6.0E−07	4.0E−05	4.0E−05	0.29	0.25/0.17	520	40	740	730	53.7
olB7_a	1.1E−06	7.0E−05	7.0E−05	0.28	0.26/0.18	570	35	840	790	52.2
olB7_b	5.5E−07	5.5E−05	5.5E−05	0.29	0.25/0.17	570	35	860	750	53.3
olB7_c	8.0E−07	9.0E−05	9.0E−05	0.29	0.27/0.18	570	50	860	790	51.1
Min	5.5E−07	1.5E−05	4.0E−05	0.22	0.18/0.13	520	35	740	730	50.9
Max	1.2E−06	1.2E−04	1.0E−03	0.31	0.27/0.18	750	70	1100	1040	56.1

Input parameters for a set of simulations (see text for detail). The rows in bold correspond to the simulations illustrated in Figs. 7 and 8. The rows in italic are simulations identical to olB2_b with the exception of CR1 that is slower or faster by one order of magnitude. Isotopic fractionation is low in both cases (see Table 3). The first value of β-Mg (0.18–0.27) and a starting δ^{26}Mg of −0.4‰ were used for the simulations but the second value of β-Mg (0.13–0.18) gives similar results with a starting δ^{26}Mg of −0.25‰ (see dark and light green lines, Figs. 7 and 8). ∅sph is the radius of the sphere of melt (of composition Mg# liq1) from which the crystal grows for stage 1 (CR1). ∅sph2 is the radius of the growth medium for stages 2 and 3 (CR2, CR3).

is interesting that in this last case the β-Fe/β-Mg is ~2 and equal to the ratio of previous studies of *in-situ* Fe-Mg isotope measurements in olivine (Sio et al., 2013; Oeser et al., 2015; Van Orman and Krawczynski, 2015).

In order to obtain a deeper understanding of model uncertainties for stage 1, the parameter space has been randomly explored for the crystallization of 3 olivine megacryst cores (olB1, olB2 and olB7). The initial composition of the core, β-Fe, β-Mg and the cooling rate were all randomly sampled. The equilibrium Mg isotopes composition was fixed to either δ^{26}Mg −0.25 or −0.4‰. About 4500 simulations were performed, 122 of which were considered to be successful (Table 4). Successful simulations produced a final Fo content equal, within ±0.5 Fo, to the composition of megacryst cores and a final δ^{26}Mg/δ^{56}Fe within ±0.12‰ of their isotopic compositions. Only the simulations that satisfied simultaneously those 3 criteria were selected. The average and standard deviation of each model parameter for the different sets of simulations are reported in Table 4. This analysis also constrains more quantitatively the uncertainty associated with the model outputs. Overall, the results are consistent with the simulations shown in Figs. 7 and 8 and summarized in Tables 2 and 3, for which the parameters were manually adjusted. The parameters associated with the crystallization of megacryst rims and subsequent cooling (stages 2 and 3) were not extensively explored and therefore remain poorly constrained. Due to the large beam size (40 μm), only 1–2 measurements could be performed in megacryst rims. Isotope fractionation in megacryst rims cannot be sufficiently resolved to justify the random sampling of the large number of parameters associated with stages 2 and 3. Stages 2 and 3 have a minimal influence on the chemical and isotopic composition at the center of olivine megacrysts (Figs. 7C and EA3) and can be ignored to constrain the parameters relevant for stage 1.

The model also makes the assumption that crystal growth is not interrupted between crystallization of the core and the rim and that the temperature decreased linearly during both crystallization stages. The implicit assumption is that no replenishment of the magma chamber significantly changed the composition of the residual melt or increased the temperature of the magma. The megacrysts were never partly resorbed and diffusion never paused (equilibrium) or reversed (bulk transfer of Mg from the liquid to the olivine). If the crystallization history deviated significantly from those assumptions, the modeled durations calculated here would represent lower limits.

The complex P (and Al) zoning of olivine megacrysts that is observed in an increasing number of olivine-phyric shergottites (Peslier et al., 2010; Shearer et al., 2013; Ennis and McSween, 2014; Liu et al., 2016) is sometimes interpreted as evidence for initial dendritic growth (Ennis

Table 3
Model outputs.

	Mg# liq2 mol.%	Fo core1 mol.%	Fo core2 mol.%	ΔFo mol.%	Fo rim mol.%	δ^{26}Mg core	δ^{56}Fe core	δ^{26}Mg rim	δ^{56}Fe rim	F res wt.%	t core years	t rim days	t diff days	t rim tot days
olA1_a	28.4	77.2	72.8	4.3	53.8	0.15	−0.81	0.82	−1.26	0.52	7.1	21	78	99
olA1_b	**28.4**	**77.2**	**73.1**	**4.0**	**53.7**	**0.15**	**−0.88**	**0.61**	**−1.08**	**0.58**	**6.0**	**15**	**59**	**74**
olA2_b	30.2	77.1	73.4	3.7	55.9	0.11	−0.72	0.30	−0.71	0.56	5.4	76	15	92
olA2_a	**29.9**	**76.9**	**73.5**	**3.4**	**55.5**	**0.10**	**−0.71**	**0.27**	**−0.67**	**0.56**	**4.9**	**57**	**5**	**62**
olA2_c	31.5	77.1	73.4	3.6	57.4	0.07	−0.82	0.40	−0.67	0.55	5.9	22	49	71
olA4_a	27.2	78.5	72.9	5.6	51.6	0.15	−0.84	0.66	−1.05	0.59	4.3	39	13	52
olB1_a	30.1	77.3	73.9	3.5	55.6	0.09	−0.75	0.45	−0.90	0.62	5.6	16	60	76
olB1_b	**31.9**	**78.0**	**73.8**	**4.1**	**57.7**	**0.10**	**−0.79**	**0.50**	**−1.03**	**0.58**	**7.4**	**25**	**109**	**134**
olB2_a	31.7	76.6	72.4	4.2	57.4	0.06	−0.67	0.25	−0.71	0.64	5.8	18	98	116
olB2_b	**30.8**	**76.6**	**72.3**	**4.3**	**56.4**	**0.05**	**−0.64**	**0.40**	**−0.84**	**0.63**	**6.6**	**20**	**88**	**108**
olB2_bs	*30.9*	*76.6*	*69.5*	*7.2*	*56.5*	*−0.26*	*−0.17*	*0.34*	*−0.75*	*0.63*	*66.0*	*20*	*88*	*108*
olB2_bf	*29.7*	*76.6*	*75.9*	*0.7*	*55.1*	*−0.21*	*−0.34*	*0.45*	*−0.91*	*0.62*	*0.7*	*20*	*867*	*887*
olB2_c	28.8	76.4	72.5	3.9	56.7	0.00	−0.64	0.34	−0.88	0.65	5.9	19	81	100
olB5_a	29.8	74.7	71.2	3.6	55.2	0.13	−0.69	0.58	−0.97	0.68	3.2	18	80	98
olB5_b	30.8	74.7	70.8	3.9	56.4	0.12	−0.67	0.64	−1.07	0.65	4.2	25	122	147
olB5_c	30.6	76.9	70.9	5.9	56.3	0.10	−0.64	0.68	−1.11	0.64	8.2	27	121	147
olB7_a	29.7	75.8	71.6	4.2	55.2	0.26	−0.82	0.64	−0.94	0.62	4.5	13	68	82
olB7_b	29.3	76.6	71.5	5.1	54.9	0.09	−0.64	0.77	−1.17	0.56	8.3	22	86	108
olB7_c	28.1	74.9	71.3	3.6	53.3	0.12	−0.62	0.72	−0.98	0.62	4.7	14	52	66
Min	28.1	74.7	70.8	3.4	53.3	0.00	−0.88	0.25	−1.26	0.52	3.2	13	5	52
Max	31.9	78.0	73.9	5.9	57.7	0.26	−0.62	0.77	−0.67	0.68	8.3	76	122	147

Mg# liq2: Final composition of the liquid. Fo core 1: Initial composition of olivine. Fo core 2: Final composition of megacryst cores. Fo rim: Final composition of megacryst rims. δ^{26}Mg/ δ^{56}Fe core: isotope fractionation reached at the center of olivine megacrysts. δ^{26}Mg/ δ^{56}Fe rim: maximal isotope fractionation reached in megacryst rims (variable position, see Figs. 7 and 8). F res: fraction of residual liquid (1 – ol crystallized). t core: time elapsed during core crystallization. t rim: time elapsed during rim crystallization (overgrowth) t diff: time elapsed during diffusion only phase.
t tot: t rim + t diff. Profiles for simulations in bold are in Figs. 7 and 8. Other profiles are in Fig. EA4.

Table 4
Average of model parameters and results from random sampling.

		δ^{26}Mg start	# of runs	CR1 (°C/s)	σ	t (years)*	t (years)**	β-Fe	σ	β-Mg	σ	Δ Fo	σ
Range	Min			7.00E−08				0.12		0.08		0	
	Max			3.00E−06				0.32		0.28		8.7	
olB2		−0.4	37	1.20E−06	4.29E−07	2.1–4.3	1.6–9.8	0.269	0.021	0.214	0.030	3.160	0.944
olB2		−0.25	31	1.25E−06	4.61E−07	1.9–3.9	1.5–9.7	0.279	0.024	0.147	0.036	3.072	0.900
olB1		−0.25	28	1.20E−06	3.41E−07	2.2–3.9	1.8–6.4	0.296	0.017	0.160	0.039	3.140	0.647
olB7		−0.25	33	1.59E−06	4.88E−07	1.7–3.2	1.4–5.7	0.273	0.022	0.148	0.034	3.523	0.767

Range min/max: Parameter space sampled for all megacrysts.
ΔFo is the difference between the initial and final forsterite content at the center of the megacryst.
* Duration of core crystallization calculated for 1 standard deviation on CR1.
** Duration calculated for 2σ on CR1.

and McSween, 2014; Welsch et al., 2014) although solute trapping resulting from growth rate changes and the slow diffusion of P in the melt are also possible (e.g. Watson and Müller, 2009; Shearer et al., 2013). There is a possibility that olivine dendrites formed a skeleton that would have been subsequently filled as olivine continued to crystallize (e.g. Shea et al., 2015). In this case, olivine megacrysts do not fully crystallize in a concentric manner and melt inclusions can easily be entrapped. The progressive filling of a dendritic skeleton would most likely results in more effective diffusion, as the liquid-crystal interface would have larger total surface area. This source of uncertainty is difficult to quantify but it is clear that any deviation of the olivine megacrysts from the morphology of a perfect sphere would make diffusion more efficient and shorten the duration of megacryst core crystallization (stage 1).

Due to the absence of correlation between the diffusivity and chemical zoning (Fig. 6), the crystallographic orientation was not taken into account to calculate diffusivities in the model. The diffusivity is calculated along the *c*-axis and we consider that the highest diffusivity is the one controlling the composition of megacryst cores. This could also lead to underestimate the duration of stages 1–3. A 3-D model would be necessary to test this model assumption.

4.4. Timescales of NWA 1068 crystallization

The simulation results of the diffusion and crystallization model confirm that megacryst cores have been rehomogenized and that the current forsterite content is 3.2 (±1.3) mol% lower than the nuclei that grew to form olivine megacrysts (2σ on olB1, Table 4). Sio and Dauphas (2016) recently reinterpreted the results of Sio et al. (2013) with a model of simultaneous diffusion and crystallization that share many similarities with the model described here. Interestingly, they also concluded that olivine megacrysts from Kilauea Iki lava lake were rehomogenized and that the Fo content of one olivine core could have been lowered by ~3 units of Fo. It also appears that the most magnesium-rich olivine megacrysts in NWA 1068 were also the richest in Fo before rehomegenization (Fig. 9). Prior to rehomogenization, olivine had a range of Fo contents (74.5–78), which suggests that they started to crystallize at different times and that nucleation has initially been continuous.

All the successful simulations require a relatively slow cooling rate of 0.05–0.13 °C/day (Tables 2–4) during the crystallization of megacryst cores. The megacryst rims crystallized much faster with a cooling rate of 5–10 °C/day (Table 3). However, this cooling rate is more difficult to constrain and, depending on the model assumptions, the total uncertainty could be larger than one order of magnitude. According to our model, the total time elapsed between the beginning of olivine nucleation and the final emplacement of the magma is 1.8–6.4 years (2σ on olB1, Table 4), which is similar to the crystal residence time in many terrestrial basalts (e.g. de Maisonneuve et al., 2016). If crystallization started near the base of the crust (40–85 km on Mars; Zuber, 2001; Genova et al., 2016), we can calculate the average ascent rate of NWA 1068 magma:

1.9×10^{-4} to 1.5×10^{-3} m/s (0.7–5.4 m/h). Those values are low relative to average magma ascent rates (e.g. Wilson and Head, 1981; Rutherford, 2008) and are probably indicative that the ascent was not continuous but, instead, that the magma pooled in the martian crust. As the magma traveled upward, some megacrysts collided, stuck together due to surface tension, and intergrew to form glomerocryts (Fig. 2). This process is known as synneusis (e.g. Vance, 1969) and is characteristic of magmatic turbulence during transport or convection in a magma chamber.

The pyroxene crystals with the highest Mg concentration (Mg# 71) are not in equilibrium with the most Mg-rich olivine but with Fo_{68} (assuming a Kd olivine-pigeonite of 1.2; Longhi and Pan, 1989). Fo_{68} corresponds approximately to the composition of olivine megacrysts before the outermost part of the rim (~50 μm) starts to crystallize in our model (Fig. 7C). Diffusion continually affected the outer rims and the olivine of the groundmass as they crystallized, lowering their Fo contents. On the other hand, we propose that the initial composition of pyroxene was mostly preserved as Fe-Mg interdiffusion coefficients in pyroxenes are 2 orders of magnitude lower than in olivine (e.g. Dohmen et al., 2016). Therefore, pyroxene and olivine from the groundmass started to crystallize simultaneously with megacryst outer rims. Plagioclase quickly joined the crystallizing assemblage and the viscosity of the magma increased drastically as the melt fraction dropped under 50% (Marsh, 1981). The time elapsed during the second and third stages of the model (100 ± 40 days) likely encompasses the final step of ascent and an episode of stationary cooling when the viscosity reached a critical value.

4.5. Parental melt of NWA 1068 and implications for the origin of enriched shergottites

The parental melts of several olivine-phyric shergottites have been estimated using the "phenocryst matching test" (BVSP, 1981; Filiberto and Dasgupta, 2011). This test assumes that phenocryst cores represent the composition of the first crystal that formed in the parental melt. As the Fe-Mg equilibrium between silicate melts and olivine is known (Toplis, 2005; Filiberto and Dasgupta, 2011), the Mg# of the parental melt can be predicted (Fig. 10). If the Mg# of the bulk rock is equal to this prediction, the bulk rock composition is assumed to be representative of the parental melt. While some shergottites have been recognized as possible parental melts (e.g. Musselwhite et al., 2006; Gross et al., 2011), NWA 1068 has been suspected to contain up to 20% of accumulated olivine (Filiberto et al., 2010), which represents the total fraction of olivine in NWA 1068 (Barrat et al., 2002). However, this test is only valid if we assume perfect fractional crystallization with no solid-liquid partial equilibration by diffusion during crystal growth. Our simulations show that even the most Mg-rich megacrysts were rehomogenized by 3.2 ± 1.3 Fo units. In consequence, accumulation of olivine is no longer required to reach Fe-Mg equilibrium and NWA 1068 could represent the composition of the parental melt (Fig. 10). The olivine compositions in equilibrium with primary martian mantle melts vary from Fo_{76} for melting of the primitive martian mantle (Collinet et al., 2015) to Fo_{85} for the mantle source of the depleted shergottites (Musselwhite et al., 2006). The parental melt of NWA 1068 could have been in equilibrium with $Fo_{80\pm1}$ olivines and would represent a primary melt of a mantle source with an intermediate Mg#. Alternatively, the parental melt could have been affected by early crystallization of olivine, which was removed from the magma. In this case, NWA 1068 would derive from a mantle source with an even higher Mg#, potentially equal to the Mg# of depleted shergottites.

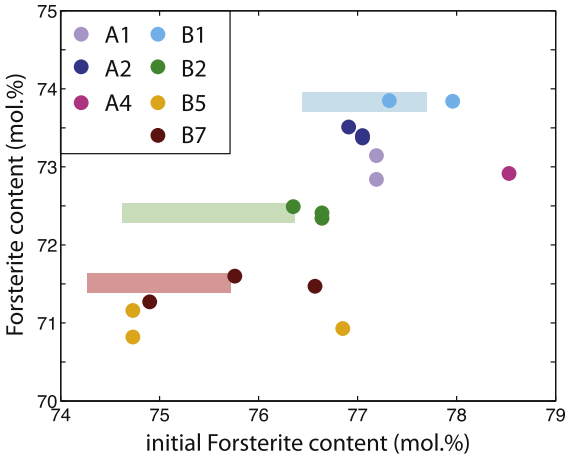

Fig. 9. Comparison of the initial forsterite content of olivine as predicted by the model (x-axis) and the actual current forsterite content measured. The result of 2 or 3 simulations are represented for the 7 olivine megacrysts for which isotopic measurements are available. The color bars represent the 1σ of the simulations in Table 4 (random search). (For interpretation of the references to color in this figure legend, the reader is referred to the web version of this article.)

If the parental melt of NWA 1068 is near-primary, it should be saturated with mineral phases characteristic of a mantle residue. Experiments performed from the whole-rock composition of NWA 1068 (Filiberto et al., 2010) have identified a multiple saturation point (MSP) where olivine and orthopyroxene appear on the liquidus of NWA 1068 at 1.7 GPa and 1520 °C. Under those conditions, the primitive martian mantle is expected to contain only olivine and orthopyroxene (Collinet et al., 2015). The CaO/Al_2O_3 of NWA 1068 is super-chondritic and rules out that the parental melt derives from the primitive martian mantle by equilibrium melting. Nonetheless, the parental melt of NWA 1068 could be near-primary and derived from a refractory mantle source, which was affected by several events of melting.

The meteorite LAR 06319 displays many similarities with NWA 1068. Both are enriched olivine-phyric shergottites, have the same bulk composition (Barrat et al., 2002; Basu Sarbadhikari et al., 2009), the same range of Fo content (~72–77) in olivine megacryst cores and rims (~50–58), and both crystallized over the same range of redox conditions (Herd, 2003, 2006; Peslier et al., 2010). Megacrysts in LAR 06319 were probably rehomogenized (Balta et al., 2013) and affected by a similar cooling history. If this is

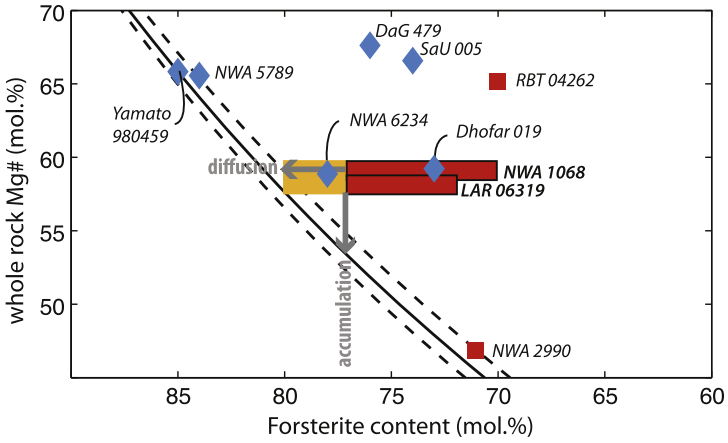

Fig. 10. Representation of the Fe-Mg equilibrium between whole-rock composition and the composition of olivine megacrysts for depleted (blue diamond) and enriched (red squares) shergottites. The dashed lines encompass Kd Fe-Mg olivine-pyroxene values in the range 0.34–0.36 (solid line is 0.35). NWA 1068 and LAR 06319 are represented as rectangles to account for the variable composition of megacryst cores. The orange extension of those rectangles toward the left (equilibrium conditions) represents the effect of diffusion. When diffusion is taken into account, no accumulation of megacryst is required to reach the equilibrium conditions. Data from Basu Sarbadhikari et al. (2009), Bunch et al. (2009), Goodrich (2003), Gross et al. (2011, 2013), Peslier et al. (2010), Taylor et al. (2002), Usui et al. (2008, 2010) and Wadhwa et al. (2001). (For interpretation of the references to color in this figure legend, the reader is referred to the web version of this article.)

the case, the bulk rock composition of LAR 06319 is also likely to reach Fe-Mg equilibrium once the composition of megacryst cores is corrected for diffusion. The main difference is the larger average crystal size of LAR 06319 groundmass relative to NWA 1068, which suggests that both shergottites may have crystallized at slightly different conditions but in the same overall environment.

We thus infer that NWA 1068 and LAR 06319 originated from similar parental melts and that the olivine megacrysts crystallized under similar conditions. Just as Yamato 980459 and NWA 5789 likely represent parental melts from which other depleted shergottites are derived (Gross et al., 2011; Rapp et al., 2013), there is a strong possibility that the whole group of enriched shergottites originates from a parental melt similar in composition to LAR 06319 and NWA 1068. Whether the enriched signature is already acquired in the mantle source of this parental melt or was overprinted later is out of the scope of this study.

5. CONCLUSIONS

The anti-correlated fractionation of Fe and Mg isotopes indicates that olivine megacrysts in NWA 1068 formed during an early, 2–6 year-long, stage of crystallization and were progressively rehomogenized by the evolving liquid in which they crystallized. However, the olivine megacrysts did not significantly accumulate and the bulk rock composition of NWA 1068 is likely representative of the parental melt. During a second, ~100 day-long, stage of crystallization, the residual melt formed the groundmass and megacryst rims as the magma was transported to its shallower site of emplacement. NWA 1068 and LAR 06319 likely share the same source and crystallization history. Their bulk compositions are identical and they are good candidates for the parental melt from which the other enriched shergottites are derived. This parental melt could be near-primary and in equilibrium with a refractory martian mantle (Mg# > 80) composed of olivine and orthopyroxene.

ACKNOWLEDGMENTS

NWA 1068 samples were made available from the collection of the "Laboratoire de Géologie de Lyon" funded by INSU and ENS. MC was an Aspirant Fellow of the Belgian Fund for Scientific Research-FNRS and was supported by a short-term DAAD research grant when this study was conducted. Part of this work was funded by a grant from the PNP program of CNRS-INSU to EM. BC is a Research Associate of the Belgian Fund for Scientific Research-FNRS. ON acknowledges support from a Marie-Curie individual fellowship. This manuscript was significantly improved from the comments of Arya Udry and two anonymous reviewers. We also thank Stephanie Brown for her helpful comments.

APPENDIX A. SUPPLEMENTARY MATERIAL

Supplementary data associated with this article can be found, in the online version, at http://dx.doi.org/10.1016/j.gca.2017.03.029.

REFERENCES

Anand M., Russell S. S., Blackhurst R. L. and Grady M. M. (2006) Searching for signatures of life on Mars: an Fe-isotope perspective. *Philos. Trans. Roy. Soc. B: Biol. Sci.* **361**, 1715–1720.

Aoudjehane H. C., Avice G., Barrat J.-A., Boudouma O., Chen G., Duke M. J. M., Franchi I. A., Gattacceca J., Grady M. M., Greenwood R. C., Herd C. D. K., Hewins R., Jambon A., Marty B., Rochette P., Smith C. L., Sautter V., Verchovsky A., Weber P. and Zanda B. (2012) Tissint Martian Meteorite: a fresh look at the interior, surface, and atmosphere of mars. *Science* **338**, 785–788.

Balta J. B., Sanborn M., McSween H. Y. and Wadhwa M. (2013) Magmatic history and parental melt composition of olivine-phyric shergottite LAR 06319: Importance of magmatic degassing and olivine antecrysts in Martian magmatism. *Meteorit. Planet. Sci.*, 1359–1382.

Balta J. B., Sanborn M. E., Udry A., Wadhwa M. and McSween H. Y. (2015) Petrology and trace element geochemistry of Tissint, the newest shergottite fall. *Meteorit. Planet. Sci.* **50**, 63–85.

Barrat J. A., Jambon A., Bohn M., Gillet P., Sautter V., Gopel C., Lesourd M. and Keller F. (2002) Petrology and chemistry of the picritic shergottite North West Africa 1068 (NWA 1068). *Geochim. Cosmochim. Acta* **66**, 3505–3518.

Basu Sarbadhikari A., Day J. M. D., Liu Y., Rumble D. and Taylor L. A. (2009) Petrogenesis of olivine-phyric shergottite Larkman Nunatak 06319: implications for enriched components in martian basalts. *Geochim. Cosmochim. Acta* **73**, 2190–2214.

Basu Sarbadhikari A., Goodrich C. A., Liu Y., Day J. M. D. and Taylor L. A. (2011) Evidence for heterogeneous enriched shergottite mantle sources in Mars from olivine-hosted melt inclusions in Larkman Nunatak 06319. *Geochim. Cosmochim. Acta* **75**, 6803–6820.

Bouvier A., Blichert-Toft J. and Albarede F. (2009) Martian meteorite chronology and the evolution of the interior of Mars. *Earth Planet. Sci. Lett.* **280**, 285–295.

Buening D. K. and Buseck P. R. (1973) Fe-Mg lattice diffusion in olivine. *J. Geophys. Res.* **78**, 6852–6862.

Bunch T. E., Irving A. J., Wittke J. H., Rumble, III, D., Korotev R. L., Gellissen M. and Palme H. (2009) Petrology and composition of Northwest Africa 2990; a new type of fine-grained, enriched, olivine-phyric shergottite. In *40th Lunar and Planetary Science Conference*, abstract 2274.

BVSP (1981) *Experimental Petrology of Basalts and Their Source Rocks. Basaltic Volcanism on the Terrestrial Planets*. Pergamon Press Inc, New York, p. 1286.

Chakrabarti R. and Jacobsen S. B. (2010) The isotopic composition of magnesium in the inner Solar System. *Earth Planet. Sci. Lett.* **293**, 349–358.

Chakraborty S., Farver J. R., Yund R. A. and Rubie D. C. (1994) Mg tracer diffusion in synthetic forsterite and San Carlos olivine as a function of P, T and fO2. *Phys. Chem. Miner.* **21**, 489–500.

Collinet M., Médard E., Charlier B., Vander Auwera J. and Grove T. L. (2015) Melting of the primitive martian mantle at 0.5–2.2 GPa and the origin of basalts and alkaline rocks on Mars. *Earth Planet. Sci. Lett.* **427**, 83–94.

Costa F. and Chakraborty S. (2004) Decadal time gaps between mafic intrusion and silicic eruption obtained from chemical zoning patterns in olivine. *Earth Planet. Sci. Lett.* **227**, 517–530.

Costa F. and Dungan M. (2005) Short time scales of magmatic assimilation from diffusion modeling of multiple elements in olivine. *Geology* **33**, 837–840.

Costa F., Dohmen R. and Chakraborty S. (2008) Time scales of magmatic processes from modeling the zoning patterns of crystals. *Rev. Mineral. Geochem.* **69**, 545–594.

Dauphas N., Roskosz M., Alp E. E., Neuville D. R., Hu M. Y., Sio C. K., Tissot F. L. H., Zhao J., Tissandier L., Médard E. and Cordier C. (2014) Magma redox and structural controls on iron isotope variations in Earth's mantle and crust. *Earth Planet. Sci. Lett.* **398**, 127–140.

Dauphas N., Teng F.-Z. and Arndt N. T. (2010) Magnesium and iron isotopes in 2.7 Ga Alexo komatiites: Mantle signatures, no evidence for Soret diffusion, and identification of diffusive transport in zoned olivine. *Geochim. Cosmochim. Acta* **74**, 3274–3291.

de Maisonneuve C. B., Costa F., Huber C., Vonlanthen P., Bachmann O. and Dungan M. A. (2016) How do olivines record magmatic events? Insights from major and trace element zoning. *Contrib. Miner. Petrol.* **171**, 1–20.

Debaille V., Yin Q. Z., Brandon A. D. and Jacobsen B. (2008) Martian mantle mineralogy investigated by the 176Lu–176Hf and 147Sm–143Nd systematics of shergottites. *Earth Planet. Sci. Lett.* **269**, 186–199.

Dohmen R., Becker H.-W. and Chakraborty S. (2007) Fe–Mg diffusion in olivine I: experimental determination between 700 and 1200 °C as a function of composition, crystal orientation and oxygen fugacity. *Phys. Chem. Miner.* **34**, 389–407.

Dohmen R. and Chakraborty S. (2007) Fe–Mg diffusion in olivine II: point defect chemistry, change of diffusion mechanisms and a model for calculation of diffusion coefficients in natural olivine. *Phys. Chem. Miner.* **34**, 409–430.

Dohmen R., Ter heege J. H., Becker H.-W. and Chakraborty S. (2016) Fe-Mg interdiffusion in orthopyroxene. *Am. Miner.* **101**, 2210–2221.

Dreibus G. and Wanke H. (1985) Mars, a volatile-rich planet. *Meteoritics* **20**, 367–381.

Ennis M. E. and McSween H. Y. (2014) Crystallization kinetics of olivine-phyric shergottites. *Meteorit. Planet. Sci.* **49**, 1440–1455.

Filiberto J., Chin E., Day J. M. D., Franchi I. A., Greenwood R. C., Gross J., Penniston-Dorland S. C., Schwenzer S. P. and Treiman A. H. (2012) Geochemistry of intermediate olivine-phyric shergottite Northwest Africa 6234, with similarities to basaltic shergottite Northwest Africa 480 and olivine-phyric shergottite Northwest Africa 2990. *Meteorit. Planet. Sci.*, 1256–1273.

Filiberto J. and Dasgupta R. (2011) Fe2+-Mg partitioning between olivine and basaltic melts: Applications to genesis of olivine-phyric shergottites and conditions of melting in the Martian interior. *Earth Planet. Sci. Lett.* **304**, 527–537.

Filiberto J., Musselwhite D. S., Gross J., Burgess K., Le L. and Treiman A. H. (2010) Experimental petrology, crystallization history, and parental magma characteristics of olivine-phyric shergottite NWA 1068: Implications for the petrogenesis of "enriched" olivine-phyric shergottites. *Meteorit. Planet. Sci.* **45**, 1258–1270.

Filiberto J., Treiman A. H. and Le L. (2008) Crystallization experiments on a Gusev Adirondack basalt composition. *Meteorit. Planet. Sci.* **43**, 1137–1146.

Genova A., Goossens S., Lemoine F. G., Mazarico E., Neumann G. A., Smith D. E. and Zuber M. T. (2016) Seasonal and static gravity field of Mars from MGS, Mars Odyssey and MRO radio science. *Icarus* **272**, 228–245.

Goodrich C. A. (2002) Olivine-phyric martian basalts: a new type of shergottite. *Meteorit. Planet. Sci.* **37**, B31–B34.

Goodrich C. A. (2003) Petrogenesis of olivine-phyric shergottites Sayh Al Uhaymir 005 and elephant moraine A79001 lithology A. *Geochim. Cosmochim. Acta* **67**, 3735–3772.

Gross J., Treiman A. H., Filiberto J. and Herd C. D. K. (2011) Primitive olivine-phyric shergottite NWA 5789: Petrography, mineral chemistry, and cooling history imply a magma similar to Yamato-980459. *Meteorit. Planet. Sci.* **46**, 116–133.

Gross J., Filiberto J., Herd C. D. K., Daswani M. M., Schwenzer S. P. and Treiman A. H. (2013) Petrography, mineral chemistry, and crystallization history of olivine-phyric shergottite NWA 6234: A new melt composition. *Meteorit. Planet. Sci.*, n/a-n/a.

Herd C. D. K. (2003) The oxygen fugacity of olivine-phyric martian basalts and the components within the mantle and crust of Mars. *Meteorit. Planet. Sci.* **38**, 1793–1805.

Herd C. D. K. (2006) Insights into the redox history of the NWA 1068/1110 martian basalt from mineral equilibria and vanadium oxybarometry. *Am. Miner.* **91**, 1616–1627.

Huebner J. S. (1971) Buffering techniques for hydrostatic systems at elevated pressures. In *Research Techniques for High Pressure and High Temperature* (ed. G. C. Ulmer). Springer, Berlin Heidelberg, Berlin, Heidelberg, pp. 123–177.

Jackson S. E. (2008) LAMTRACE data reduction software for LA-ICP-MS. In *Laser ablation-ICP-mass spectrometry in the Earth sciences: Current practices and outstanding issues. Mineralogical Association of Canada Short Course Series* (ed. P. Sylvester), pp. 305–307. Laser ablation-ICP-mass spectrometry in the Earth sciences: Current practices and outstanding issues. Mineralogical Association of Canada Short Course Series.

Jambon A. (1980) Isotopic fractionation: A kinetic model for crystals growing from magmatic melts. *Geochim. Cosmochim. Acta* **44**, 1373–1380.

Jambon A., Sautter V., Barrat J. A., Gattacceca J., Rochette P., Boudouma O., Badia D. and Devouard B. (2016) Northwest Africa 5790: Revisiting nakhlite petrogenesis. *Geochim. Cosmochim. Acta* **190**, 191–212.

Jochum K. P., Willbold M., Raczek I., Stoll B. and Herwig K. (2005) Chemical characterisation of the USGS reference glasses GSA-1G, GSC-1G, GSD-1G, GSE-1G, BCR-2G, BHVO-2G and BIR-1G Using EPMA, ID-TIMS, ID-ICP-MS and LA-ICP-MS. *Geostand. Geoanal. Res.* **29**, 285–302.

Jones J. H. (2015) Various aspects of the petrogenesis of the Martian shergottite meteorites. *Meteorit. Planet. Sci.* **50**, 674–690.

Koizumi E., Mikouchi T., Monkawa A. and Miyamoto M. (2004) Origin of olivine in megacrysts and the groundmass crystallization of the Dar al Gani 476 shergottite. *Antarct. Meteor. Res.* **17**, 84–96.

Lazarov M. and Horn I. (2015) Matrix and energy effects during in-situ determination of Cu isotope ratios by ultraviolet-femtosecond laser ablation multicollector inductively coupled plasma mass spectrometry. *Spectrochim. Acta, Part B* **111**, 64–73.

Liu Y., Baziotis I. P., Asimow P. D., Bodnar R. J. and Taylor L. A. (2016) Mineral chemistry of the Tissint meteorite: Indications of two-stage crystallization in a closed system. *Meteorit. Planet. Sci.*, n/a–n/a.

Longerich H. P., Jackson S. E. and Gunther D. (1996) Inter-laboratory note. Laser ablation inductively coupled plasma mass spectrometric transient signal data acquisition and analyte concentration calculation. *J. Anal. At. Spectrom.* **11**, 899–904.

Longhi J. and Pan V. (1989) The parent magmas of the SNC meteorites. In *Procedings of the 19th Lunar and Planetary Science Conference*, pp. 451–464.

Magna, T.H.Y., Teng, F.-Z., Mezger, K., 2017. Magnesium isotope systematics of SNC meteorites: evidence for crystal fractionation or surface process? 48th Lunar and Planetary Science Conference, abstract 1795.

Marsh B. D. (1981) On the crystallinity, probability of occurrence, and rheology of lava and magma. *Contrib. Miner. Petrol.* **78**, 85–98.

Marsh B. D. (1988) Crystal size distribution (CSD) in rocks and the kinetics and dynamics of crystallization. *Contrib. Miner. Petrol.* **99**, 277–291.

McSween H. Y. and Jarosewich E. (1983) Petrogenesis of the Elephant Moraine A79001 meteorite: Multiple magma pulses on the shergottite parent body. *Geochim. Cosmochim. Acta* **47**, 1501–1513.

Mikouchi T. and Miyamoto M. (2002) Olivine cooling rate of the northwest Africa 1068 shergottite. In *33th Lunar and Planetary Science Conference*, abstract 1346.

Mikouchi T., Miyamoto M. and McKay G. A. (2001) Mineralogy and petrology of the Dar al Gani 476 martian meteorite: implications for its cooling history and relationship to other shergottites. *Meteorit. Planet. Sci.* **36**, 531–548.

Miyamoto M., Mikouchi T., Satake W., Koizumi E. and Kaiden H. (2010) The cooling rate of several olivine-phyric shergottites on the basis of Fe-Mg zoning in olivine. In *41st Lunar and Planetary Science Conference*, abstract 1143.

Monders A. G., Medard E. and Grove T. L. (2007) Phase equilibrium investigations of the Adirondack class basalts from the Gusev plains, Gusev crater, Mars. *Meteorit. Planet. Sci.* **42**, 131–148.

Moser D. E., Chamberlain K. R., Tait K. T., Schmitt A. K., Darling J. R., Barker I. R. and Hyde B. C. (2013) Solving the Martian meteorite age conundrum using micro-baddeleyite and launch-generated zircon. *Nature* **499**, 454–457.

Musselwhite D. S., Dalton H. A., Kiefer W. S. and Treiman A. H. (2006) Experimental petrology of the basaltic shergottite Yamato-980459: Implications for the thermal structure of the Martian mantle. *Meteorit. Planet. Sci.* **41**, 1271–1290.

Norman M. D., Yaxley G. M., Bennett V. C. and Brandon A. D. (2006) Magnesium isotopic composition of olivine from the Earth, Mars, Moon, and pallasite parent body. *Geophys. Res. Lett.* **33**, L15202.

O'Neill H. S. C. (1987) Quartz-fayalite-iron and quartz-fayalite-magnetite equilibria and the free energy of formation of fayalite (Fe_2SiO_4) and magnetite (Fe_3O_4). *Am. Miner.* **72**, 67–75.

Oeser M., Weyer S., Horn I. and Schuth S. (2014) High-precision Fe and Mg isotope ratios of silicate reference glasses determined in situ by femtosecond LA-MC-ICP-MS and by solution nebulisation MC-ICP-MS. *Geostand. Geoanal. Res.* **38**, 311–328.

Oeser M., Dohmen R., Horn I., Schuth S. and Weyer S. (2015) Processes and time scales of magmatic evolution as revealed by Fe–Mg chemical and isotopic zoning in natural olivines. *Geochim. Cosmochim. Acta* **154**, 130–150.

Peslier A. H., Hnatyshin D., Herd C. D. K., Walton E. L., Brandon A. D., Lapen T. J. and Shafer J. T. (2010) Crystallization, melt inclusion, and redox history of a Martian meteorite: Olivine-phyric shergottite Larkman Nunatak 06319. *Geochim. Cosmochim. Acta* **74**, 4543–4576.

Peters T. J., Simon J. I., Jones J. H., Usui T., Moriwaki R., Economos R. C., Schmitt A. K. and McKeegan K. D. (2015) Tracking the source of the enriched martian meteorites in olivine-hosted melt inclusions of two depleted shergottites, Yamato 980459 and Tissint. *Earth Planet. Sci. Lett.* **418**, 91–102.

Poitrasson F. and Freydier R. (2005) Heavy iron isotope composition of granites determined by high resolution MC-ICP-MS. *Chem. Geol.* **222**, 132–147.

Poitrasson F., Halliday A. N., Lee D.-C., Levasseur S. and Teutsch N. (2004) Iron isotope differences between Earth, Moon, Mars and Vesta as possible records of contrasted accretion mechanisms. *Earth Planet. Sci. Lett.* **223**, 253–266.

Rapp J. F., Draper D. S. and Mercer C. M. (2013) Anhydrous liquid line of descent of Yamato-980459 and evolution of Martian parental magmas. *Meteorit. Planet. Sci.*, 1780–1799.

Richter F., Chaussidon M., Mendybaev R. and Kite E. (2016) Reassessing the cooling rate and geologic setting of Martian meteorites MIL 03346 and NWA 817. *Geochim. Cosmochim. Acta* **182**, 1–23.

Richter F. M., Liang Y. and Davis A. M. (1999) Isotope fractionation by diffusion in molten oxides. *Geochim. Cosmochim. Acta* **63**, 2853–2861.

Richter F. M., Davis A. M., DePaolo D. J. and Watson E. B. (2003) Isotope fractionation by chemical diffusion between molten basalt and rhyolite. *Geochim. Cosmochim. Acta* **67**, 3905–3923.

Rutherford M. J. (2008) Magma ascent rates. *Rev. Mineral. Geochem.* **69**, 241–271.

Schmidt M. E. and McCoy T. J. (2010) The evolution of a heterogeneous Martian mantle: Clues from K, P, Ti, Cr, and Ni variations in Gusev basalts and shergottite meteorites. *Earth Planet. Sci. Lett.* **296**, 67–77.

Shafer J. T., Brandon A. D., Lapen T. J., Righter M., Peslier A. H. and Beard B. L. (2010) Trace element systematics and (super 147) Sm/ (super 143) Nd and (super 176) Lu/ (super 176) Hf ages of Larkman Nunatak 06319; closed system fractional crystallization of an enriched shergottite magma. *Geochim. Cosmochim. Acta* **74**, 7307–7328.

Shea T., Lynn K. J. and Garcia M. O. (2015) Cracking the olivine zoning code: Distinguishing between crystal growth and diffusion. *Geology* **43**, 935–938.

Shearer C. K., McKay G., Papike J. J. and Karner J. M. (2006) Valence state partitioning of vanadium between olivine-liquid: Estimates of the oxygen fugacity of Y980459 and application to other olivine-phyric martian basalts. *Am. Miner.* **91**, 1657–1663.

Shearer C. K., Burger P. V., Papike J. J., Borg L. E., Irving A. J. and Herd C. (2008) Petrogenetic linkages among Martian basalts: Implications based on trace element chemistry of olivine. *Meteorit. Planet. Sci.* **43**, 1241–1258.

Shearer C. K., Aaron P. M., Burger P. V., Guan Y., Bell A. S. and Papike J. J. (2013) Petrogenetic linkages among fO_2, isotopic enrichments-depletions and crystallization history in Martian basalts. Evidence from the distribution of phosphorus in olivine megacrysts. *Geochim. Cosmochim. Acta* **120**, 17–38.

Shih, C.-Y., Nyquist, L.E., Wiesmann, H., Barrat, J.A., 2003. Age and Petrogenesis of Picritic Shergottite NWA1068: Sm-Nd and Rb-Sr Isotopic Studies. 34th Lunar and Planetary Science Conference, abstract 1439.

Shirai N. and Ebihara M. (2004) Chemical characteristics of a Martian meteorite, Yamato 980459. *Antarct. Meteorite Res.* **17**, 55–67.

Sio C. K. I. and Dauphas N. (2016) Thermal and crystallization histories of magmatic bodies by Monte Carlo inversion of Mg-Fe isotopic profiles in olivine. *Geology*. http://dx.doi.org/10.1130/G38056.1.

Sio C. K. I., Dauphas N., Teng F.-Z., Chaussidon M., Helz R. T. and Roskosz M. (2013) Discerning crystal growth from diffusion profiles in zoned olivine by in situ Mg–Fe isotopic analyses. *Geochim. Cosmochim. Acta* **123**, 302–321.

Sossi P. A., Nebel O., Anand M. and Poitrasson F. (2016) On the iron isotope composition of Mars and volatile depletion in the terrestrial planets. *Earth Planet. Sci. Lett.* **449**, 360–371.

Steinhoefel G., Horn I. and von Blanckenburg F. (2009) Matrix-independent Fe isotope ratio determination in silicates using UV femtosecond laser ablation. *Chem. Geol.* **268**, 67–73.

Sugawara T. (2000) Empirical relationships between temperature, pressure, and MgO content in olivine and pyroxene saturated liquid. *J. Geophys. Res.: Solid Earth* **105**, 8457–8472.

Taylor G. J. (2013) The bulk composition of Mars. *Chem. Erde* **73**, 401–420.

Taylor L. A., Nazarov M. A., Shearer C. K., McSween H. Y., Cahill J., Neal C. R., Ivanova M. A., Barsukova L. D., Lentz R. C., Clayton R. N. and Mayeda T. K. (2002) Martian meteorite Dhofar 019: A new shergottite. *Meteorit. Planet. Sci.* **37**, 1107–1128.

Teng F.-Z., Dauphas N., Helz R. T., Gao S. and Huang S. (2011) Diffusion-driven magnesium and iron isotope fractionation in Hawaiian olivine. *Earth Planet. Sci. Lett.* **308**, 317–324.

Teng F.-Z., Li W.-Y., Ke S., Yang W., Liu S.-A., Sedaghatpour F., Wang S.-J., Huang K.-J., Hu Y., Ling M.-X., Xiao Y., Liu X.-M., Li X.-W., Gu H.-O., Sio C. K., Wallace D. A., Su B.-X., Zhao L., Chamberlin J., Harrington M. and Brewer A. (2015) Magnesium isotopic compositions of international geological reference materials. *Geostand. Geoanal. Res.* **39**, 329–339.

Toplis M. J. (2005) The thermodynamics of iron and magnesium partitioning between olivine and liquid: criteria for assessing and predicting equilibrium in natural and experimental systems. *Contrib. Miner. Petrol.* **149**, 22–39.

Usui T., McSween H. Y. and Floss C. (2008) Petrogenesis of olivine-phyric shergottite Yamato 980459, revisited. *Geochim. Cosmochim. Acta* **72**, 1711–1730.

Usui T., Sanborn M., Wadhwa M. and McSween H. Y. (2010) Petrology and trace element geochemistry of Robert Massif 04261 and 04262 meteorites, the first examples of geochemically enriched lherzolitic shergottites. *Geochim. Cosmochim. Acta* **74**, 7283–7306.

Van Orman J. A. and Krawczynski M. J. (2015) Theoretical constraints on the isotope effect for diffusion in minerals. *Geochim. Cosmochim. Acta* **164**, 365–381.

Vance J. A. (1969) On synneusis. *Contrib. Miner. Petrol.* **24**, 7–29.

Wadhwa M., Lentz R. C. F., McSween H. Y. and Crozaz G. (2001) A petrologic and trace element study of Dar al Gani 476 and Dar al Gani 489: Twin meteorites with affinities to basaltic and lherzolitic shergottites. *Meteorit. Planet. Sci.* **36**, 195–208.

Wang K., Moynier F., Dauphas N., Barrat J.-A., Craddock P. and Sio C. K. (2012) Iron isotope fractionation in planetary crusts. *Geochim. Cosmochim. Acta* **89**, 31–45.

Watson E. B. (1996) Surface enrichment and trace-element uptake during crystal growth. *Geochim. Cosmochim. Acta* **60**, 5013–5020.

Watson E. B. and Müller T. (2009) Non-equilibrium isotopic and elemental fractionation during diffusion-controlled crystal growth under static and dynamic conditions. *Chem. Geol.* **267**, 111–124.

Welsch B., Hammer J. and Hellebrand E. (2014) Phosphorus zoning reveals dendritic architecture of olivine. *Geology*. http://dx.doi.org/10.1130/G35691.1.

Weyer S., Anbar A. D., Brey G. P., Münker C., Mezger K. and Woodland A. B. (2005) Iron isotope fractionation during planetary differentiation. *Earth Planet. Sci. Lett.* **240**, 251–264.

Weyer S. and Schwieters J. B. (2003) High precision Fe isotope measurements with high mass resolution MC-ICPMS. *Int. J. Mass Spectrom.* **226**, 355–368.

Weyer S. and Seitz H. M. (2012) Coupled lithium- and iron isotope fractionation during magmatic differentiation. *Chem. Geol.* **294–295**, 42–50.

Wiechert U. and Halliday A. N. (2007) Non-chondritic magnesium and the origins of the inner terrestrial planets. *Earth Planet. Sci. Lett.* **256**, 360–371.

Wilson L. and Head J. W. (1981) Ascent and eruption of basaltic magma on the Earth and Moon. *J. Geophys. Res.: Solid Earth* **86**, 2971–3001.

Zhang Y., Ni H. and Chen Y. (2010) Diffusion data in silicate melts. *Rev. Mineral. Geochem.* **72**, 311–408.

Zipfel J., Scherer P., Spettel B., Dreibus G. and Schultz L. (2000) Petrology and chemistry of the new shergottite Dar al Gani 476. *Meteorit. Planet. Sci.* **35**, 95–106.

Zuber M. T. (2001) The crust and mantle of Mars. *Nature* **412**, 220–227.

Associate editor: Shichun Huang